FINITE ELEMENT SIMULATION OF THE COMPACTION AND SPRINGBACK OF AN ALUMINUM POWDER METALLURGY ALLOY

by

Stanley Gerald Selig

Submitted in partial fulfilment of the requirements
for the degree of Master of Applied Science

at

Dalhousie University
Halifax, Nova Scotia
March 2012

DALHOUSIE UNIVERSITY

DEPARTMENT OF MECHANICAL ENGINEERING

The undersigned hereby certify that they have read and recommend to the Faculty of Graduate Studies for acceptance a thesis entitled "FINITE ELEMENT SIMULATION OF THE COMPACTION AND SPRINGBACK OF AN ALUMINUM POWDER METALLURGY ALLOY" by Stanley Gerald Selig in partial fulfilment of the requirements for the degree of Master of Applied Science.

Dated: March 22, 2012

Supervisor: _____

Readers: _____

_____

DALHOUSIE UNIVERSITY

DATE: March 22, 2012

AUTHOR: Stanley Gerald Selig

TITLE: Finite Element Simulation of the Compaction and Springback of an Aluminum Powder Metallurgy Alloy

DEPARTMENT OR SCHOOL: Department of Mechanical Engineering

DEGREE: MASc CONVOCATION: May YEAR: 2012

Signature of Author

To my family, and to all the friends with whom I've shared these last few years.

Table of Contents

List of Tables

List of Figures

Abstract

A new finite element model was developed to predict the density distribution in an Alumix 321 powder metallurgy compact. The model can predict the density distribution results of single-action compaction from 100 to 500 MPa compaction pressure. The model can also determine the amount of springback experienced by a compact upon ejection from the die at 100 and 300 MPa compaction pressure. An optical densitometry method, along with the creation of a compaction curve, was used to experimentally predict density distributions found within compacts, and found results that were consistent with both literature and finite element simulation. Further powder characterization included testing apparent density and flow rate of the powder. A literature review was also conducted and the results of which have been organized by three categories (powder type, material model, and finite element code) for easy reference by future powder researchers.

List of Abbreviations and Symbols Used

Roman Symbol	Description
A	Shima-Oyane model parameter
B	Shima-Oyane model parameter
D	Drucker-Prager hardening law exponent
d	Diameter of test cylinder in determination of compaction curve
DPC	Drucker-Prager Cap
DWF	Die wall friction
FE	Finite element
h	Height of test cylinder in determination of compaction curve
IPF	Inter-particle friction
J_1	First invariant of the stress tensor
J_{2D}	Second invariant of the deviatoric stress tensor
$L(\kappa)$	Drucker-Prager hardening cap location variable
m_A	Mass of powder in apparent density test
m_G	Mass of test cylinder in determination of compaction curve
MPIF	Metal Powder Industries Federation
p	Hydrostatic pressure
PM	Powder metallurgy
R	Drucker-Prager cap surface axis ratio
V	Final volume of powder compact
V_0	Initial volume of powder compact
V_A	Volume of powder in apparent density test
W	Drucker-Prager hardening law coefficient
$X(\kappa)$	Drucker-Prager hardening cap location variable
Y_o	Yield strength for fully-dense material for Shima-Oyane model
$Y_{\gamma,so}$	Yield strength for given relative density for Shima-Oyane model

Greek Symbol	Description
α	Drucker-Prager model failure envelope parameter
β	Drucker-Prager model failure envelope exponent
γ	Failure envelope exponential coefficient
γ_{so}	Relative density of powder compact for Shima-Oyane model
δ	Shima-Oyane model parameter
δ_{ij}	Kronecker delta
ε_v^p	Effective volumetric plastic strain
θ	Drucker-Prager model failure envelope linear coefficient
κ	Drucker-Prager model hardening parameter
ν	Poisson's ratio
ρ_A	Arnold apparent density
ρ_G	Green density of test cylinder in determination of compaction curve
$\rho_{rel,0}$	Initial relative density of powder compact
$\rho_{rel,f}$	Final relative density of powder compact
$\sigma_1, \sigma_2, \sigma_3$	Principal normal stresses
σ_{ij}	Stress tensor
σ'_{ij}	Deviatoric stress tensor
σ_{nn}	Hydrostatic stress
σ_{tresca}	Tresca stress
σ_{vm}	Von Mises stress
$\sigma_x, \sigma_y, \sigma_z$	Normal stresses in given direction
σ_Y	Yield strength
$\tau_{12}, \tau_{13}, \tau_{23}$	Shear stresses associated with principal stresses
$\tau_{xy}, \tau_{xz}, \tau_{yz}$	Shear stresses in given direction

Acknowledgements

I must acknowledge a large number of people, without whom I would not have produced the following document:

Geoffrey Beck, for all his extremely valuable help along the way. Dr. Darrel Doman, for his ever-present guidance. Dr. Paul Bishop, and the members of his research group (Randy, Boland, and Winston) for the use and instruction of the PM lab. Dr. Kevin Plucknett, for the use of his microscope and image software. Carmen McKnight, Braden Murphy, Matthew Harding, and all other members and guests of the T-Building just for generally being awesome people. Rogue's Roost, for being such a gracious host of lab meetings, and last but not least, the T-Room for all the great memories during the course of my degrees.

Chapter 1: Introduction

Powder metallurgy (PM) is a manufacturing method in which powdered metal is consolidated into a component of a desired shape. This process can be performed using several methods, and most utilize a pressing (compaction) step and a heat-treating step (sintering). Known as the "press-and-sinter" technique, conventional methods use a rigid die and punch set which compacts powdered metal uniaxially until it becomes a cohesive component, after which it is sintered to increase the strength of the part. PM manufacturing processes generate parts that are near net shape; that is, the components that are produced need little to no secondary machining to achieve the final dimensions.

Powder compaction is a critical step in the PM process since the overall performance of a PM part is largely based on the quality of the compaction. The quality of a compact can be quantified by the densification of the part, where the focus is on the

distribution of the local densities. Strength and other material properties increase with density, so it is important that the part is both dense and uniform after the compaction step. If there are large variations in the density found throughout a part, low-density areas will be weak points in the compact, and will lead to a reduced overall quality of a part (German, 2005).

Aluminum PM (Al PM) is a fast-growing segment of the PM industry as automotive manufacturers look to reduce the overall weight of vehicles by replacing a range of ferrous PM components, and thus increase their fuel efficiency; Anderson and Foley (2001) discuss some of the work being done to advance the state of Al PM manufacturing methods to make mass-production a reality and Huo *et al.* (2009) suggested that PM aluminums are feasible substitutes in the place of both die-cast aluminum and ferrous PM materials for moving engine components. As strength and other material properties increase with density, the reliability of PM parts is affected by both the bulk density and density gradients within the green compacts. Similarly, the dimensional tolerance of the final compact is affected by warping during sintering as well as the elastic springback experienced by the green compact upon ejection from the die (German, 2005). It is for these reasons that this work investigates the density distribution and springback found within PM parts.

There are many phenomena that occur during the compaction process that deal with the mechanics of powder compaction, and therefore research has focused on several

particular aspects of the process. Some of the major areas of research in terms of powder compaction phenomena include die wall friction and the effects of lubrication (admixed and sprayed on die wall) on the final state of the compact (Rahman *et al.*, 2011; Zhou *et al.*, 2002; Ngai *et al.*, 2002; Li *et al.*, 2002; Brown *et al.*, 1999), and accurately modelling metal powder behaviour in terms of the densification mechanics during compaction (Rahman *et al.*, 2011; Lee and Kim, 2002; Coube and Riedel, 2000). These phenomena are often difficult to measure experimentally, but finite element (FE) analysis can provide researchers with detailed information: forces at the die-powder interface, internal plastic strains, pressure transmission through the powder, and others.

This work first presents a detailed description of the tools and continuum mechanics that are used in the study of PM compaction, followed by a literature review of the work that has been done on the FE simulation of PM compaction. The experimental setups and FE models used to investigate the compaction and springback of an aluminum powder (ECKA Granules' Alumix 321) will then be introduced. Results of each will be shown and compared, and conclusions will be drawn about the results of the experimental and simulation work.

Chapter 2: Background

This chapter will discuss three major facets of PM compaction, and the finite element simulation thereof:

1. Compaction techniques
2. Die compaction theory
3. Material models

2.1 Compaction Techniques

Powder compaction is used extensively in industry to produce high volumes of parts with almost no wasted material. The main powder compaction techniques are uniaxial die compaction, metal injection molding and cold and hot isostatic pressing. In research facilities, triaxial die compaction is also used to make compacts under tightly controlled constraints which allows the researcher to characterize the powder densification behaviour; this technique is not used in commercial pressing of parts.

The focus of this work is on uniaxial die compaction, in which a punch compresses powder in a rigid-walled die. This can be modified by changing the configuration of the punches and their movement schedules. In single-action compaction the lower punch is fixed and the upper punch is lowered to compress the powder, whereas in double-action compaction both punches are moved and apply load to the powder. This technique can also involve several upper and lower punches that move at different times/speeds in order to create a multi-level part.

Isostatic pressing techniques use a flexible die which is sealed with powder inside, and is submerged in a fluid chamber which is then hydraulically pressurized. This technique (hot or cold) creates an even pressure from all sides of the part, which results in a more uniform density distribution.

Triaxial die compaction is a combination of both uniaxial and isostatic pressing, where a triaxial cell is pressurized around the cylinder wall with oil or some other fluid, and this cell is pressed top-to-bottom using upper and lower punches as in uniaxial compaction. This technique is typically reserved for research purposes as it gives a true indication of the powder densification qualities. As such, it is most often used to develop material parameters that drive FE models of powder compaction. However, it is a difficult and time consuming method where few setups are in active use and have pressure capabilities suitable for determining metal powder parameters (Pavier and Doremus, 1999; Menzies, 1988; MACE3 Lab, 2012).

2.2 Die Compaction Theory

2.2.1 Powder Consolidation

Compaction, in general terms, compresses powder particles together, reducing the amount of empty space found between particles in a loose powder. The compaction process usually follows the same general steps in terms of densification of the powder, where Figure 1 presents a schematic of the steps of densification.

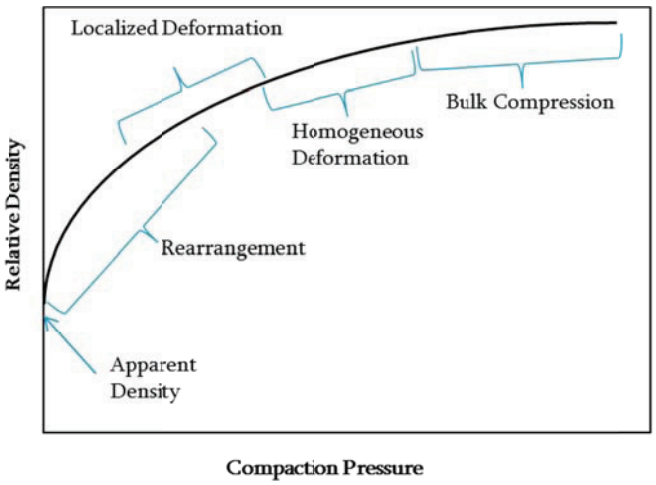

Figure 1 - Densification events in powder compaction (adapted from German, 1994)

First, the particles themselves begin to rearrange themselves into a more tightly-packed configuration, resulting in a rapid increase of density. Once the particles are as tightly-packed as possible, the point contacts between particles begin to deform under the compaction pressure and the number of particles touching a given particle increases. The homogeneous deformation stage now begins and the voids between particles start to collapse, and the particles begin to take on a polygonal shape as the plastic deformation sets in. The particles are now becoming work hardened and

brittle. The bulk deformation stage of compaction offers very little in terms of increasing density of the green compact, with only the collapse of very small pores.

Another aspect of die compaction which needs to be considered is the effect of die-wall friction. In a simple uniaxial die compaction scenario, there are two main configurations: single-action and double-action compaction (Figure 2). In a single-action compaction die, only one punch (upper or lower) acts on the powder, while the other remains stationary which means the pressure is applied at one end of the compact.

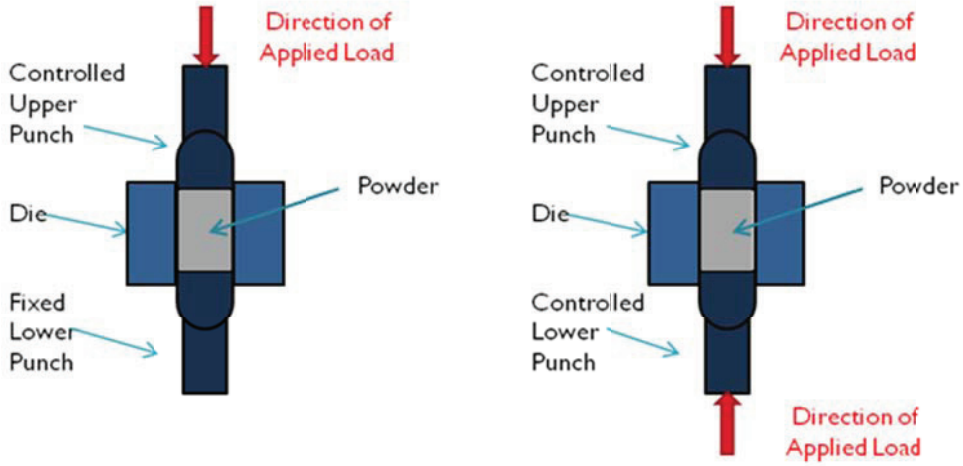

Figure 2 - Schematic of single- and double-action compaction

2.2.2 Lubrication

Due to die wall friction (DWF) and inter-particle friction (IPF), the pressure is not transmitted all the way to the bottom of the compact in a single-action scenario. In double-action compaction, the press applies the load with both punches, which serves

to increase uniformity and overall density in the powder compact as the pressure transmission distance is reduced.

Die compaction generally results in density gradients in the green compact. As shown in Figure 3, single-action compaction results in a high-low density gradient from the point of pressing to the passive end, while double-action compaction sees a density "split" occur at a location between the presses depending on the load from each press. Also note that the lowest density in the single-action compaction scenario is substantially lower than the lowest density in the double-action compaction scenario. A simple copper PM cylinder is shown and the numbers shown are densities in g/cm^3.

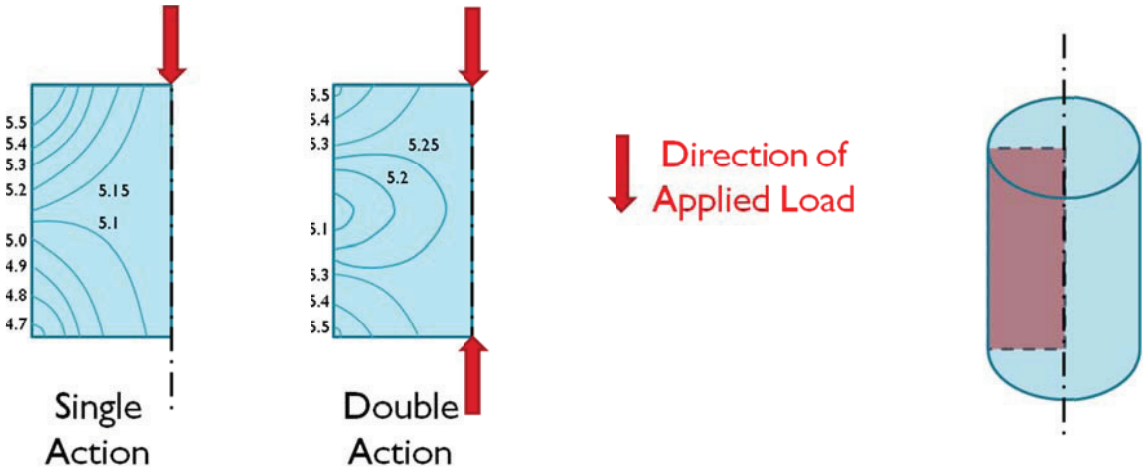

Figure 3 - Single-action versus double-action compaction in density gradients (adapted from German, 1994)

In order to minimize DWF effects, and to properly press powders, it is necessary to have a lubricant present in the process. Iron and aluminum powders often have the lubricant mixed in as part of the powder blend (generally around 0.4 - 1.5 wt%

lubricant) (German, 2005). This ensures that the particles pack together more easily during compaction, and also reduces the wear on the die walls. In addition to this, the density of the green compact is also more uniform, and the ejection process requires less force. The wax is compacted into the green compact, so before the part is sintered and moved onto secondary machining operations, the compact is raised to a high enough temperature to expel the lubricant.

An alternative method is to directly lubricate the punches and die wall using one of several techniques, including spraying (Ball *et al.*, 1995) or brushing (Li *et al.*, 2002) the lubricant onto the tooling, or electrostatic lubrication of molds (Brown *et al.*, 1999).

2.2.3 Powder Considerations

When comparing compressibility of powders in terms of green density it is important to keep in mind particle size. Smaller particles are not as able to be compressed, as it requires more energy to collapse the small pores found in finer powders. The amount of particle contact, and thus higher contact surface area, increases the IPF in the system, requiring more energy than with coarser powders. It is known that the green density of powders reaches a maximum at a blend of approximately 73% coarse particles and the remainder being fine particles (German, 2005). The particles in this mixture are better able to arrange themselves into a dense configuration, more so than fine or coarse particles on their own.

Particle morphology also has an impact on the compaction of powders. Materials that are atomized into powder form generally range from irregular and rounded (water or air atomized) to spherical (inert gas atomized) particle shapes. Materials which are hydrogen reduced and milled into powder are generally irregular, porous, and angular in shape. Figure 4 gives an example of an atomized powder and Figure 5 shows hydrogen reduced and milled powder. Note the differences mentioned above in particle shape. Particle shape plays a significant role in density and flow rate of a powder due to the amount of IPF generated between powder particles. As a general rule of thumb, the more irregular the particle shape, the lower the apparent density of the loose powder will be, and the slower the flow rate will be of a powder through an orifice. This can have an effect on the initial density distribution in the loose powder, which influences the final, compacted, density distributions. Powder particle shape also plays a large part in compressibility which is of importance in this study. Irregular powders, due to their increased IPF have a harder time compressing when compared to spherical particles of the same size.

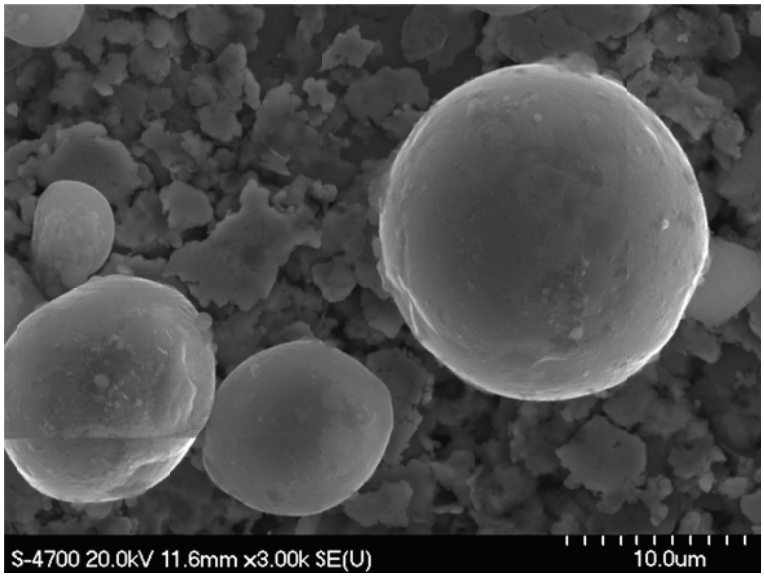

Figure 4 – Micrograph of atomized magnesium powder from scanning electron microscope

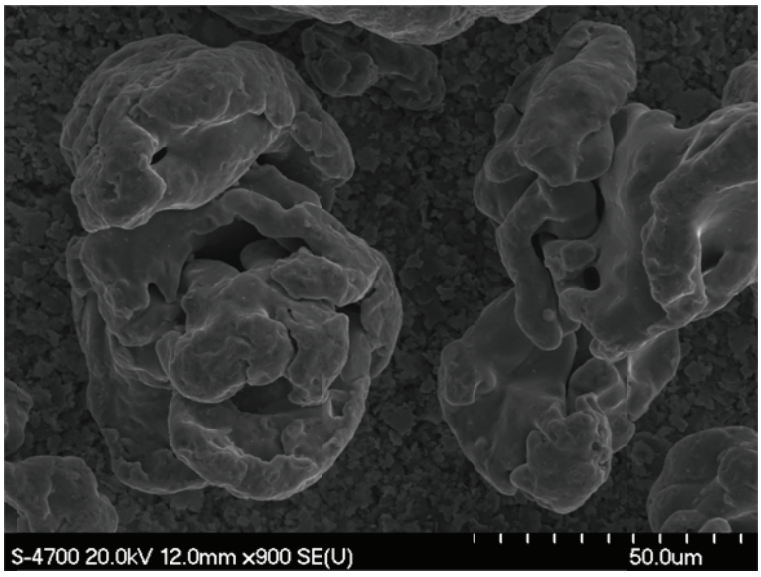

Figure 5 – Micrograph of hydrogen reduced iron powder from scanning electron microscope

Particle chemistry also plays a role in powder compaction. Elemental powders are soft and compress easily, yielding a high green density. Powders which are fabricated as pre-alloyed particles are very difficult to compress, as they have higher strength and do not deform easily. These powders are useful in that they produce components

with high mechanical properties if compressed and sintered correctly. Powders which are a mix of elemental and master alloy powders perform somewhere between the elemental and fully pre-alloyed powders mentioned above.

2.3 Material Models

This section will discuss the foundations of plasticity models, and explain in detail how several common constitutive material models work.

2.3.1 Yield Surfaces for Solid Metals

In order to understand how PM constitutive models work, it is important to first understand the concept of yielding. Yielding is a term used to describe permanent deformation of a material when it exceeds a certain state of stress. Establishing when a material will yield depends on the material properties and the loading scenario.

Under simple uniaxial testing, materials have a property known as yield strength, or σ_Y. If the stress experienced by a material is smaller than the yield strength, the material deforms elastically; that is, the material will return to its original form upon release. If this stress exceeds the yield strength, the material begins to deform plastically, or, permanently.

When a material undergoes a multiaxial state of stress, the determination of when a material will yield becomes more complicated than using a simple value of yield

strength. There are several models available to predict when a material will begin to plastically deform, and many of these models are represented by yield surfaces.

In a three-dimensional state of stress, the directional stresses are given by the normal stresses σ_x, σ_y, and σ_z, and the shear stresses τ_{xy}, τ_{xz}, and τ_{yz}. It is possible to orient the coordinate system in such a way that it results in maximum, intermediate, and minimum normal stresses σ_1, σ_2, and σ_3 respectively, known as principal stresses, along with their associated shear stresses, τ_{12}, τ_{13}, and τ_{23}.

Of the many theories that have been proposed for material yield, the ones stated here are two of the most commonly applied yield criteria. The Tresca maximal shear stress criterion (Tresca, 1864) that states that material would yield if

$$\sigma_{tresca} = \sigma_1 - \sigma_3 > \sigma_{max} \tag{1}$$

and underestimates the apparent yield strength of a material in most situations. For this reason, it is considered to be a conservative theory, erring on the safe side of yielding. The von Mises yield criterion, or distortion energy theory (von Mises, 1913),

$$\sigma_{vm} = \sqrt{\frac{1}{2}[(\sigma_1 - \sigma_2)^2 + (\sigma_1 - \sigma_3)^2 + (\sigma_2 - \sigma_3)^2 + 6(\tau_{12}^2 + \tau_{13}^2 + \tau_{23}^2)]} \tag{2}$$

is more accurate in predicting the behavior of metals in all states of stress, and as such is more prevalent in engineering applications.

In order to visualize what these yield surfaces look like, let us first look at a two dimensional state of stress. In Figure 6, the Tresca yield criterion forms an irregular hexagon on the principal $\sigma_1 - \sigma_2$ plane, and the von Mises yield criterion forms an ellipse which coincides with several key points on the Tresca curve.

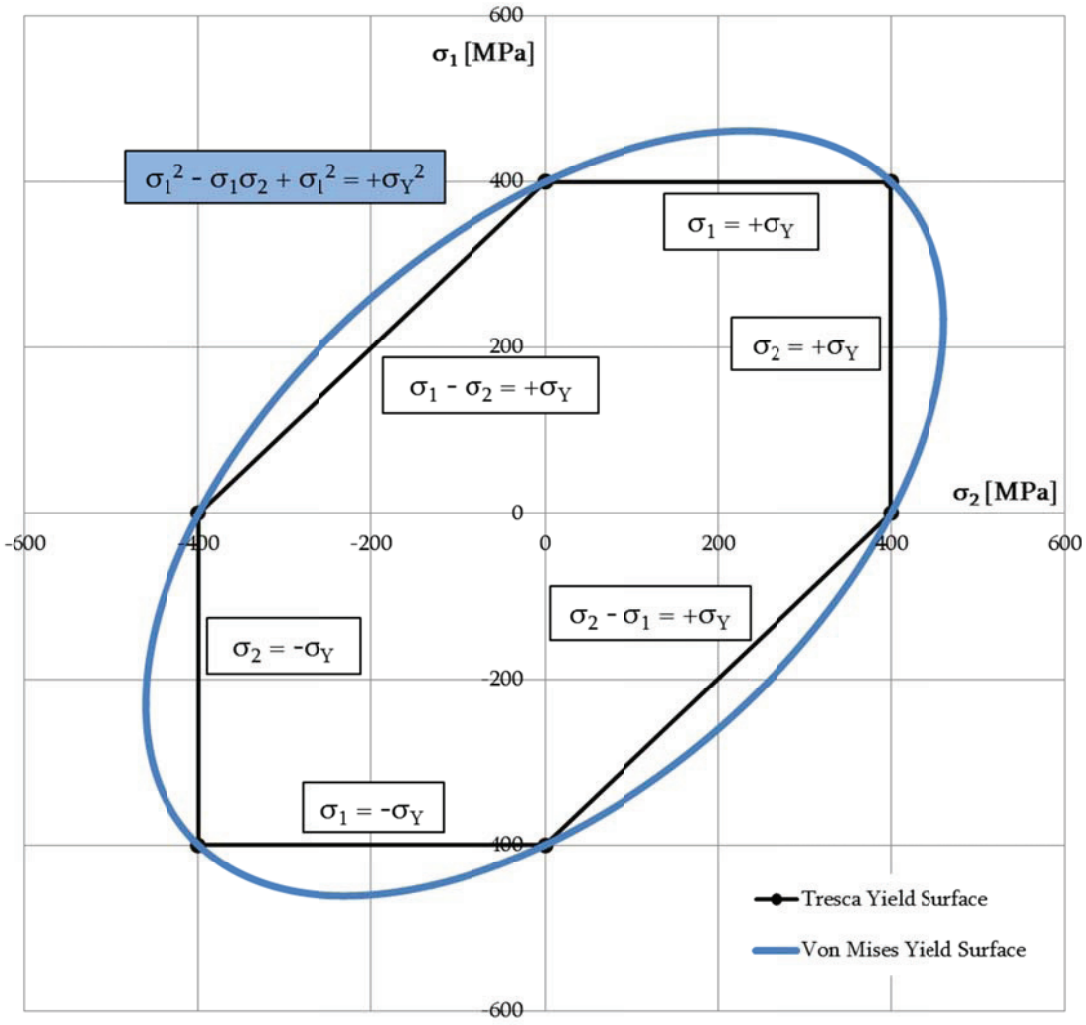

Figure 6 - Tresca and von Mises yield criteria in 2D for a material with 400 MPa yield strength

The curves shown above are also known as failure envelopes. If a state of stress is such that the plotted point lies inside the failure envelope, the metal behaves

elastically. If the state of stress results in a point outside the envelope, the metal begins to yield.

In Figure 7, various loading scenarios are illustrated and superimposed onto the failure envelopes as discussed above. The failure envelopes shown in the figure are for a metal with a yield strength of 400 MPa.

The results of these loading scenarios can be divided into two categories: instances where Tresca and von Mises predict yielding at the same state of stress, and instances where Tresca predicts yielding at a lower state of stress than von Mises.

For certain experimental tests, including standard uniaxial tensile tests, and applying tension or compression (plane stress) evenly in the perpendicular directions, it can be seen that both Tresca and von Mises predict yielding at the same state of stress. However, following a stress path of pure shear (holding a bar and applying torsion), applying a combination of uniaxial and shear loads, or applying tension or compression (plane stress) at different rates in the perpendicular directions results in Tresca indicating yielding at a lower state of stress than the more accurate von Mises. This illustrates the statement made earlier which regarded Tresca as a conservative theory, predicting yielding at lower states of stress than von Mises.

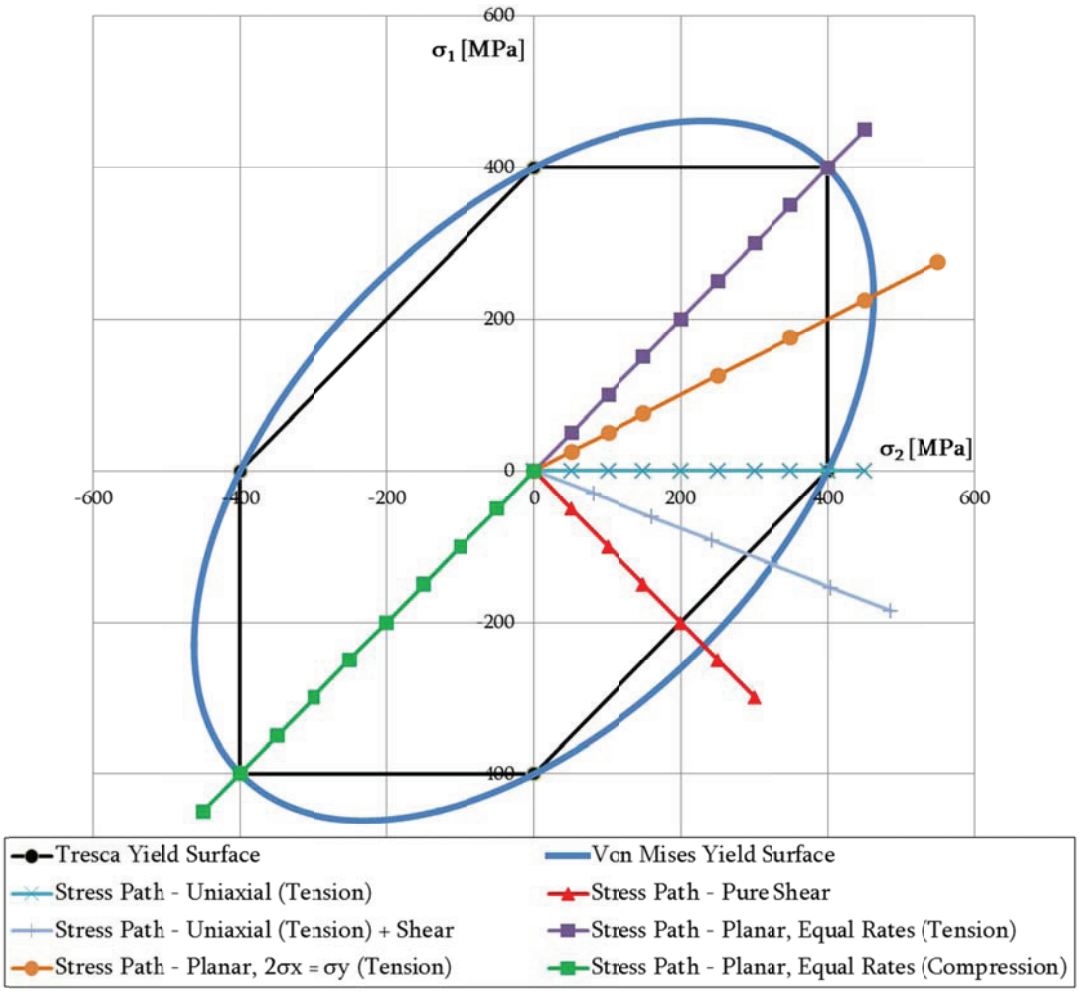

Figure 7 - Various loading paths imposed on Tresca and von Mises failure envelopes

For a fully three dimensional state of stress, our visualization of the failure envelope changes. If we visualize the three principal axes which are orthogonal to one another, then the envelope is represented by a cylinder that travels along the $\sigma_1 = \sigma_2 = \sigma_3$ line. This line can be thought of as the pressure axis. Since increasing pressure does not affect yielding of metals, the radius of the failure envelope is constant for all pressures, forming a cylindrical yield surface as seen in Figure 8. The surface normal to the pressure axis, where $\sigma_1 + \sigma_2 + \sigma_3 = 0$, is called the π-plane.

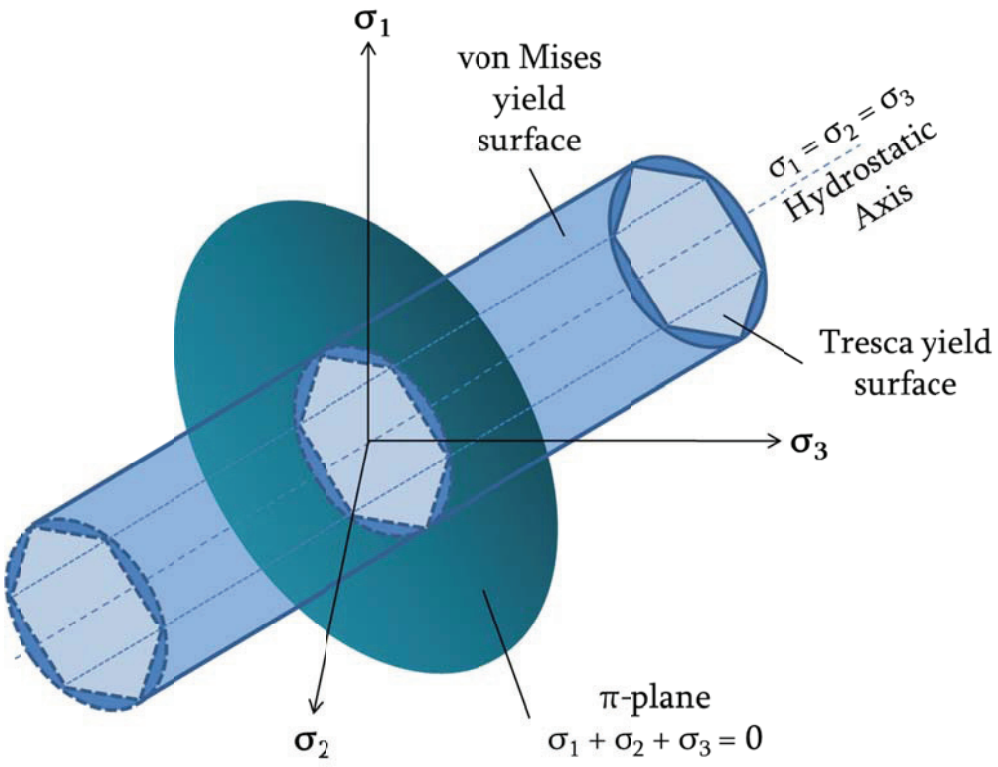

Figure 8 - von Mises yield surface in 3D

The principle is the same for the 3D cylinder as it was for the 2D ellipse, such that if a state of stress exists such that the point lies outside the cylindrical envelope on the π-plane, the metal will begin to yield.

2.3.2 Tensorial Notation of Yield Surfaces for Solid Metals

Now that Section 2.3.1 has illustrated the concept of yield surfaces, the mathematics can now be examined in preparation for a discussion of powder yield surfaces in Section 2.3.3. Note that throughout the following discussion, tensorial notation will be employed following finite element constitutive modelling practice. A 3D state of stress can be represented by a stress tensor. This stress tensor, σ_{ij}, is defined as:

$$\sigma_{ij} = \begin{pmatrix} \sigma_{11} & \sigma_{12} & \sigma_{13} \\ \sigma_{21} & \sigma_{22} & \sigma_{23} \\ \sigma_{31} & \sigma_{32} & \sigma_{33} \end{pmatrix} \quad (3)$$

Many important values relating to the above discussion can be derived from the stress tensor. The stress tensor can be decomposed into two parts: a hydrostatic portion, and a deviatoric portion. The hydrostatic portion is the uniform pressure distributed over the object (i.e. a differential cube) and has a negligible effect on plastic deformations. The deviatoric stress tensor is the main contributor to permanent deformation. This is why the cylindrical von Mises yield surface has a constant radius as the hydrostatic pressure,

$$p = \frac{1}{3}\sigma_{nn} = \frac{1}{3}(\sigma_{11} + \sigma_{22} + \sigma_{33}) \quad (4)$$

increases along the pressure axis in Figure 8. The decomposition is as follows:

$$\sigma_{ij} = \sigma'_{ij} + \frac{1}{3}\sigma_{nn}\delta_{ij} \quad (5)$$

where σ'_{ij} is the deviatoric stress tensor, σ_{nn} is the hydrostatic stress, and δ_{ij} is the Kronecker delta, or, the identity matrix. The elements contained within the diagonal of the second term of (5) are equal to one another and denote the mean pressure on the component. Another important term is the von Mises stress, σ_{vm}, which can be expressed in terms of the deviatoric stress tensor as,

$$\sigma_{vm} = \sqrt{\frac{3}{2}\sigma'_{ij}\sigma'_{ij}} \quad (6)$$

The yield criterion associated with the von Mises stress occurs when

$$\sigma_{vm} > \sigma_Y \tag{7}$$

where σ_Y is the current yield strength which would occur when the state of stress is located on the surface of the circle on the π-plane.

2.3.3 Yield Surfaces for PM Materials

Now that simple material models have been discussed in terms of yield surfaces, it is now possible to expand on this knowledge and apply it to more complex powder material models. While there are a vast number of ways in which researchers represent the behaviour of powdered metal undergoing compaction, an attempt is made here to broadly classify them into two main families: granular and porous material models. Regardless of the model type, all must simulate the densification behaviour of powdered metals which is a non-reversible plastic deformation phenomenon. A further complication, and a significant difference when compared with solid metals, is that the stiffness (*e.g.* elastic modulus) changes with densification.

When discussing yield surfaces for PM materials, two terms are used frequently when describing the yield surfaces: the first invariant of the stress tensor, J_1, which is given in (8), and the square root of the second invariant of the deviatoric stress tensor, $\sqrt{J_{2D}}$ which is given in (9).

$$J_1 = \sigma_{nn} = 3p \tag{8}$$

$$\sqrt{J_{2D}} = \sqrt{\frac{1}{2}\sigma'_{ij}\sigma'_{ij}} = \frac{1}{\sqrt{3}}\sigma_{vm} \tag{9}$$

Granular Material Models

The first family of plasticity models is for granular materials. These models include Drucker-Prager (Drucker and Prager, 1952), Mohr-Coulomb (Coulomb, 1776) and Cam-Clay (Roscoe *et al.*, 1963) among others. Granular models are able to describe material behaviour for all possible loading cases; they are not tailored for just particular loading paths (such as pure shear or axial symmetry). Furthermore, the parameters of the model may be determined using a relatively small number of standard or simple material tests, and the model is phenomenological in nature (Khoei, 2005).

A material that starts off at a low density, such as soil or PM material, will behave differently than a solid metal. Whereas increasing the hydrostatic pressure on a solid metal does not affect the yield surface shape (see Figure 8), powdered metal is greatly affected by increasing hydrostatic stress. As the powder becomes more and more dense, it begins to act more like a solid metal. Therefore, at low values of pressure, the yield strength is very low: plastic deformation occurs at very small values of stress. As the material is further compacted, the density increases, and the yield strength of the material grows. Therefore, if one were to visualize what this yield surface would

look like, it would appear to be a cone travelling along the pressure axis. As the pressure increases, the cross-section on the π-plane (see Figure 8) expands, representing an increase in yield strength. This cross-section does not expand forever; as the powder reaches maximum density, the radius reaches a maximum value, based on the type of material. Furthermore, another phenomenon is present when analyzing PM material. The particles are experiencing work hardening as the particles are being deformed, and this is represented in the model by a second surface known as a hardening cap. The cap is essentially the limit of the maximum pressure that the powder can withstand without an increase in density.

The foregoing description of material models are colloquially referred to as cap-type models. One of the most common models, the Drucker–Prager Cap (DPC) model, is shown in Figure 9. The J_1 axis of the DPC model can be thought of as being analogous to the hydrostatic axis of the von Mises model, while the $\sqrt{J_{2D}}$ axis is analogous to the radius of the cylinder (see Figure 8).

The formula for the fixed yield surface as seen in Figure 9 has many variations, but one particular version of this is the following, implemented by Sandler and Rubin (1979):

$$\sqrt{J_{2D}} + \gamma e^{-\beta J_1} - \theta J_1 - \alpha = f_1 \tag{10}$$

where α, β, γ, and θ are material model parameters, and the material is in compression. The exponential term contained within this function serves to create a plateau, which illustrates the evolution of the behavior of powdered metal to act more like a solid metal under higher states of stress.

The hardening cap is defined by the equation:

$$\sqrt{J_{2D}} - \frac{1}{R}\sqrt{[X(\kappa) - L(\kappa)]^2 - [J_1 - L(\kappa)]^2} = f_2 \tag{11}$$

where $X(\kappa)$ is the intersection of the cap surface with the J_1 axis, R is the surface axis ratio of the cap, and $L(\kappa)$ is defined as

$$L(\kappa) = \begin{cases} \kappa \text{ if } \kappa > 0 \\ 0 \text{ if } \kappa \leq 0 \end{cases} \tag{12}$$

The hardening parameter, κ, is the J_1 intersection between the Drucker-Prager yield surface and the cap surface, and is related to the plastic volumetric strain, ε_v^p, through the hardening law

$$\varepsilon_v^p = W\{1 - \exp[-D(X(\kappa) - X_0)]\} \tag{13}$$

where W and D are material model parameters.

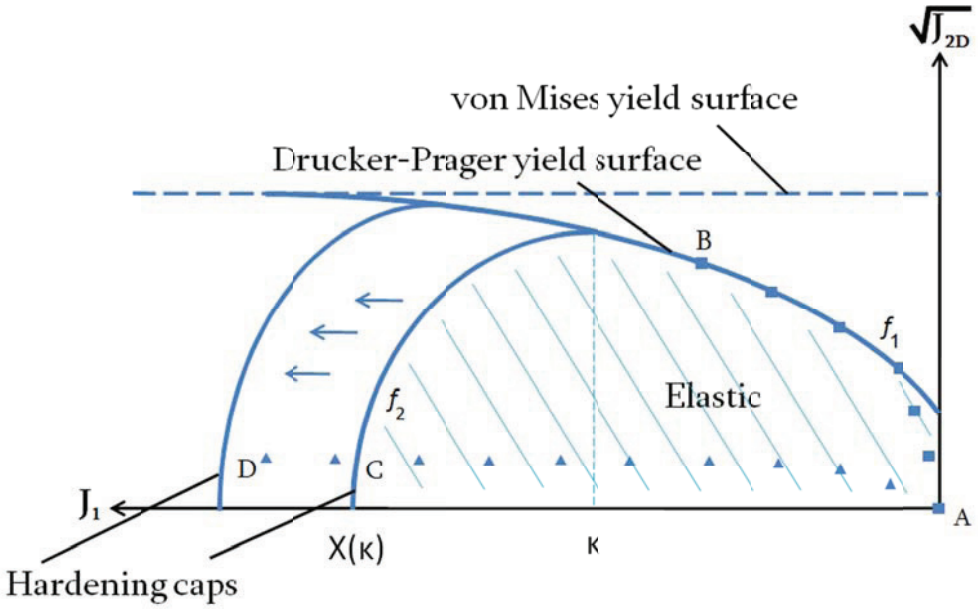

Figure 9 – Drucker–Prager Cap model visualization

As the state of stress is increased in a material governed by a DPC model, several changes to the material can occur as predicted by the model. Firstly, if the state of stress is such that it is located beneath the yield surface and before the first hardening cap, the behavior of the material will be elastic. If the state of stress increases as illustrated by stress path A-B in Figure 9, the stress path will travel until it reaches the yield surface, and the material will continue to yield as the state of stress is increased. If the state of stress increases along A-D, the material will be elastically deforming until point C, and will work-harden once it passes the first hardening cap. The hardening cap will then move further down the J_1 axis.

Porous Material Models

The second plasticity family consists of models developed for porous materials, such as Kuhn and Downey (1971), Shima-Oyane (Oyane *et al.*, 1973), and Fleck-Gurson (Fleck *et al.*, 1992; Gurson, 1977), which express the hydrostatic and deviatoric stresses in terms of the yield stress of the solid material and the yield stress of the partially dense material found in a part during compaction.

A brief description of one of the more widely-used porous models, is presented here. A schematic of the yield surface for the Shima-Oyane model is shown in Figure 10. Several variations of the parameters found in this model exist in the literature, but these models are all based on the same general equation:

$$AJ_{2D} + BJ_1^2 = \delta Y_0^2 = Y_{\gamma,so}^2 \quad \textbf{(14)}$$

where A, B, and δ are functions of the relative density of the powder (γ_{so} in Figure 10), and Y_0 and $Y_{\gamma,so}$ are the yield strengths of the solid material and partially dense material, respectively.

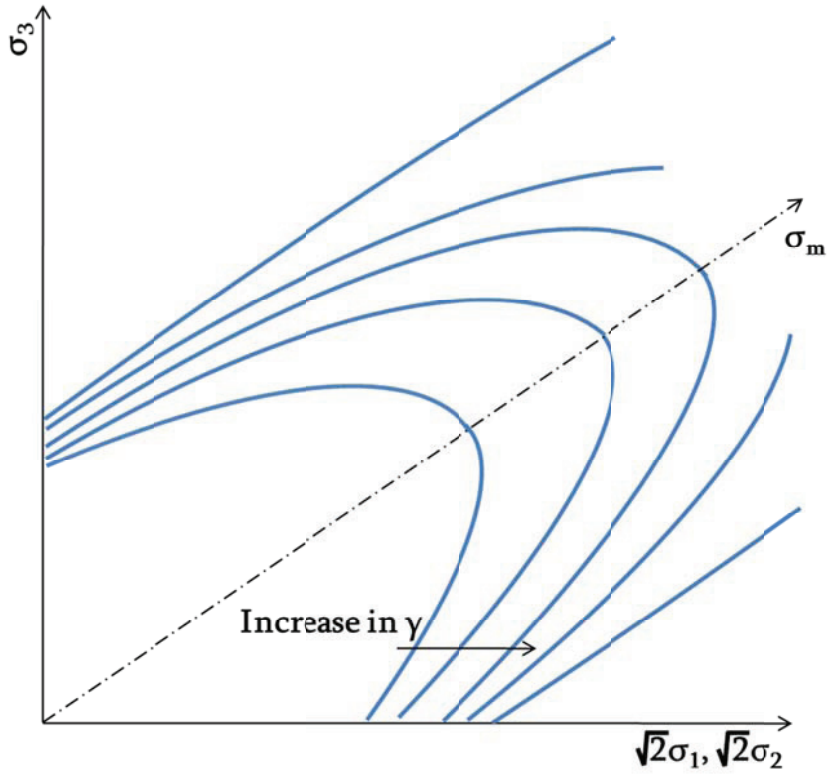

Figure 10 - Yield Surface for Shima-Oyane model (adapted from Oyane *et al.*, 1973)

However, these models make assumptions which do not hold true at very low densities (*i.e.* the start of the powder compaction process) (Khoei, 2005) and therefore its use for the simulation of a compact being created from loose powder is not suitable. When investigating pre-compacted sintered powder, this type of model is more applicable (Khoei, 2005).

Chapter 3: Literature Review

A literature review is presented here which summarizes pre-existing finite element metal powder die compaction models. As the PM field is fairly expansive, the present review aims to both provide a detailed review and highlight the areas where there is a lack of research. There are many works in the literature that deal with finite element analysis of the compaction of non-metals such as soils, sand, ceramics, and pharmaceuticals, and while there are some similarities, they were considered to be outside the scope of the research presented in this work.

Recent reviews on analytical (continuum approaches), ceramic, and pharmaceutical powders by Cunningham *et al.* (2004), Aydin *et al.* (1997), and Sinka (2007), respectively, have given a broad overview of the modelling field. However, surveys of existing modelling efforts in metallic PM applications have been somewhat limited,

where the PM Modnet's 1999 review fundamental and Calero's 2006 industry-centric reviews are standouts.

This review is separated into three categories by material: ferrous PM, non-ferrous/non-aluminum PM, and finally aluminum PM. Analysis of the literature results is presented vis-à-vis modelling approaches, and the last section investigates the papers that experimentally determined the density distribution. These results are a key action in validating compaction models.

3.1 Ferrous PM

Ferrous material is used very commonly in a wide variety of automotive components and therefore has been quite thoroughly investigated. Several experimental-only works, notably Doremus *et al.* (1995) and Pavier and Doremus (1999), characterized ferrous powders using a high pressure triaxial cell; the results of which were subsequently widely used by other FE modellers (Rahman *et al.*, 2011; Shtern and Mikhailov, 2002; Cocks, 2001). Sinka *et al.* (2000) also used a ferrous alloy powder (DistaloyAE) to study triaxial compaction as well as other tests, and compared these to the results found by Doremus *et al.* (1995) and the test results were found to be in broad agreement. Korachkin *et al.* (2008) also used DistaloyAE in experimental work which tested the effects of ad-mixed lubrication on the Young's modulus and tensile failure properties of green compacts.

The papers in the literature that focus on the simulation of iron powder compaction are sub-categorized by granular or porous material model, and a brief description of each paper is presented. Table 1 lists the PM compaction models which use iron-based powders, classified by powder type, powder material model, and FE code.

Table 1 - Literature review for ferrous PM metal

Author	Title	Material	Model Type	Year	Finite Element Code
Granular Powder Material Model					
Tran, Lewis, Gethin, Ariffin	Numerical Modelling of Powder Compaction Processes: Displacement Based Finite Element Method	Ferrous metal	Granular	1993	Unknown
Krezalek, Sivakumar	Computational Simulation of Powder Movement During Uniaxial Die Compaction of Metal Powders	Ferrous metal	Granular	1995	STRAND 6
PM Modnet Research Group	Comparison of Computer Models Representing Powder Compaction Process	Ferrous metal	Granular	1999	ABAQUS, DYNA2D
Wikman, Solimannezhad, Larsson, Oldenburg, Haggblad	Wall Friction Coefficient Estimation Through Modelling of Powder Die Pressing Experiment	Ferrous metal	Granular	2000	DYNA2D
Coube, Riedel	Numerical Simulation of Metal Powder Die Compaction with Special Consideration of Cracking	Ferrous metal	Granular	2000	ABAQUS
Doremus, Toussaint, Alvain	Simple Tests and Standard Procedure for the Characterisation of Green Compacted Powder	Ferrous metal, ceramic, other metal	Granular	2001	DYNA2D, ABAQUS
Chtourou, Guillot, Gakwaya	Modeling of the Metal Powder Compaction Process Using the Cap Model. Part I. Experimental Material Characterization and Validation, Part II. Numerical Implementation and Practical Applications	Ferrous metal	Granular	2002	ABAQUS
PM Modnet Research Group	Numerical Simulation of Powder Compaction for Two Multilevel Ferrous Parts	Ferrous metal	Granular	2002	Unknown custom and commercial codes

Author	Title	Material	Model Type	Year	Finite Element Code
Mikhailov, Shtern	Numerical Modelling of the Compaction of Powder Articles of Complex Shape in Rigid Dies: Effect of Compaction Scheme on Density Distribution II. Modelling Procedure and Analysis of Forming Schemes	Ferrous metal	Granular	2003	Unknown
Coube, Cocks, Wu	Experimental and Numerical Study of Die Filling, Powder Transfer and Die Compaction	Ferrous metal	Granular	2005	ABAQUS
Khoei, Shamloo, Azami	Extended FEM in Plasticity Forming of Powder Compaction with Contact Friction	Ferrous metal	Granular	2006	Proprietary (X-FEM)
Wikman, Bergman, Oldenburg, Haggblad	Estimation of Constitutive Parameters for Powder Pressing by Inverse Modelling	Ferrous metal	Granular	2006	DYNA2D
Khoei, Azami, Azizi	Computational Modelling of 3D Powder Compaction Processes	Ferrous metal	Granular	2007	Unknown
Liu, Xia, Zhou, Li	Numerical Simulation of Metal Powder Compaction Considering Material & Geometrical Nonlinearity	Ferrous metal	Granular	2007	MSC.Marc
Rahman, Ariffin, Nor	Development of a Finite Element Model of Metal Powder Compaction Process at Elevated Temperature	Ferrous metal	Granular	2009	Custom
Zadeh, Kim, Jeswiet	Nonlinear Finite Element Analysis of Metal Powder Die Compaction Using Various Plasticity Models	Ferrous metal	Granular	2009	ABAQUS
Porous Powder Material Model					
Weber, Brown	Simulation of the Compaction of Powder Components	Ferrous metal	Porous	1989	Unspecified (implicit, non-linear)
Svoboda, Haggblad, Nasstrom	Simulation of Hot Isostatic Pressing of Metal Powder Components to Near Net shape	Ferrous metal	Porous	1996	NIKE2D, TOPAZ2D, CACE
Kim, Cho	A Densification Model for Mixed Metal Powder Under Cold Compaction	Ferrous metal with copper mix	Porous	2001	ABAQUS
Kang, Lee, Kim	Densification Behavior of Iron Powder During Cold Stepped Compaction	Ferrous metal	Porous	2007	ABAQUS
Lee, Chung, Cho, Chung, Kwon, Kim, Joun	Three-dimensional Finite Element Analysis of Powder Compaction Process of Forming Cylinder Block of Hydraulic Pump	Ferrous metal	Porous	2008	Unknown

Author	Title	Material	Model Type	Year	Finite Element Code
Unknown Powder Material Model					
Zhu, Li, Liang, Xiang, Yin	Comparison Study of Single Direction and Friction Assisted Compaction of Multiple Alloy Powders by Finite Element Simulation	Ferrous metal	Unknown	2012	DEFORM, Newton-Raphson Solver

When looking at granular models used to model ferrous PM, the vast majority of them incorporate a hardening cap in the model. The most common granular model used in the literature is the Drucker-Prager Cap (DPC) model, followed by the Mohr-Coulomb Cap model and the Cam-Clay model.

Krezalek and Sivakumar (1995) studied the mass movement of the powder during compaction using the DPC-derived Hehenberger model in the FE simulations, and tested these results experimentally using iron powder layers separated by thin copper layers. The FE model they used predicted the stress distributions quite well, and the displacements were approximately 10-15% higher in the experiment than the FE model. The PM Modnet Research Group (1999, 2002) used both the Cam-Clay and DPC models with different finite element codes to simulate compaction of multilevel parts. The conclusion reached was that reasonable results can be derived by using different models and FE codes to describe the same material behaviour. Coube and Riedel (2000) studied the formation of cracks in compacted iron PM parts during the compaction, unloading, and ejection phases of the compaction process by using a modified DPC model. Their model is very good at predicting green density

throughout 2D and 3D multi-level parts, predicting within 0.05 g/cm^3 density in five regions of one part. Wikman *et al.* (2000) used a DPC model to model a cylindrical iron PM part, in order to investigate the wall friction coefficient as a function of relative density, and it was found that in general, the coefficient decreases as the relative density increases. Doremus *et al.* (2001) proposed a set of standard tests to fit model parameters of the DPC model. This was tested by simulating the compaction of a drawing die part and comparing the density distribution and punch forces with those determined from experimental data. The density distribution was calculated within a mean of 1%, with a maximum of 3% difference, while the punch forces simulated were within a maximum of 10% overestimation when compared to experimental data. Chtourou *et al.* (2002a) modelled an axisymmetric multi-level part and used the DPC model to try and match triaxial and isostatic loading cases from experiment, with good success. It was also found that the variables of the DPC model have a different level of influence on the results: W has the greatest influence by far, followed by the elastic modulus, then the model parameter D, then the shear modulus, with the remainder having minimal influence on the final result. They then investigated the practical industrial applications for this model and once again compared the finite element results to the experimental data with close agreement (Chtourou *et al.,* 2002b). Coube *et al.* (2005) investigated the effects of die filling on the final density distribution found within an H-shaped part. The die filling aspect was modelled with discrete element analysis, while the densification was studied

using finite element analysis with the DPC model. It was found that depressions in the top of the columns of loose powder have more of an impact on creating an inhomogeneous density distribution, when compared to the effects of initial inhomogeneity caused by powder filling. Wikman *et al.* (2006) used the DPC model to model an axisymmetric bottle-neck shape compact in DYNA2D and a pulley in ABAQUS. The pulley was shown to have good agreement with the experimental determination of density, but underestimated the density in some locations. Khoei *et al.* (2006) used a custom finite element technique to model tablet compaction, a rotated flange component, and a shaped tip component. For the latter two components, a comparison of this custom technique and traditional FE modelling is shown, and in both cases, it appears that the density contours are of similar shape, and for the most part are in good agreement, but the predicted local densities in some interface locations are not as close. Khoei *et al.* (2007) used the DPC model to model several parts in 3D and also compared a simulated triaxial test to the results from the triaxial tests performed by Doremus *et al.* (1995) and found very comparable results. A modified Cam-Clay model and a DPC model were used by Zadeh *et al.* (2009) to test two FE models. The Cam-Clay model was found to show very close agreement to experimental density distributions, and the second experiment, which took geometry from Coube and Riedel (2000), showed very good agreement when compared to the results found in the same paper.

Tran *et al.* (1993) modelled a plain bushing component using the Mohr-Coulomb Cap model, and compared the measured density at different compaction pressures against experimentally-made components of the same size and shape, with good results. Adaptive remeshing was recommended for the more complex T-section component, while it was not necessary for a straight bush component. Mikhailov and Shtern (2003) used the Cam-Clay model to study the density distribution on a multi-level part resulting from different compaction schemes with varying punch velocities and found good agreement with experiment. Rahman *et al.* (2009) used the elliptical cap model to model an axisymmetric bush component under warm compaction using a custom FE code. It was found that the simulated punch stress had good correlation with experiment, the warm compaction route provides higher green density, and springback is marginally larger in warm compaction compared to cold compaction.

The porous family of material models is the second point of discussion for ferrous powders. One of the earliest papers in the literature which studies ferrous PM as its main focus is Weber and Brown (1989) which presented in-depth mathematical constitutive equations for the material model and studied cylindrical components undergoing closed die compaction using the Kuhn and Downey model, which showed great correlation between simulation and experiment overall, but the resolution of the experimental density method (hardness testing) made it unable to accurately predict contours in areas with sharp density contours. Svoboda *et al.* (1996) used a

modified Shima-Oyane model to simulate the hot isostatic pressing of a turbine component, and compares the calculated and measured axial displacements of the component; the plastic strain at elements close to the edge in both the experiment and simulation show similar results. Kim and Cho (2001) studied the effects of varying copper powder percentages by volume mixed with tool steel powder. They performed cold isostatic pressing and single-action die compaction, and found that a mix between the Fleck and Tvergaard material models was the best fit for this powder mixture. Kang *et al.* (2007) studied the densification behaviour of a ferrous powder using the Shima-Oyane model during the cold stepped compaction of a hollow cylinder using die compaction, and cold isostatic pressing. Hardness testing was used to determine the density distribution experimentally, and this was in good agreement with the finite element simulation. Liu *et al.* (2007) modelled a cylinder of iron powder using the Ellipsoidal model, citing the complexity of cap models as not being cost-effective and opting instead to use the simpler Ellipsoidal model which is derived from the von Mises model. Lee *et al.* (2008) uses, among other models, the Shima-Oyane material model, stating that from their findings, it is a better choice than granular models such as Cam-Clay and the modified Drucker-Prager model.

Most recently, Zhu *et al.* (2012) studied the difference between single-action and friction assisted compaction (an approximation of double-action compaction using

relative die wall motion) using an unknown material model and found results which were consistent with literature.

3.2 Non-Ferrous/Non-Aluminum PM Metals

In the literature, several groups have investigated the compaction of non-ferrous, non-aluminum metals and alloys, although in some cases, the authors do not specify the type of metal being studied. Table 2 lists the literature that includes research on non-ferrous, non-aluminum metals, sorted by material type. The discussion following Table 2 is sorted by granular material models followed by porous material models.

Table 2 - Literature review for non-ferrous, non-aluminum PM metal

Author	Title	Material	Model Type	Year	Finite Element Code
Tran, Lewis, Gethin, Ariffin	Numerical Modelling of Powder Compaction Processes: Displacement Based Finite Element Method	Bronze, Ceramic, Carbon	Granular	1993	Unknown
Smith, Midha, Graham	Simulation of Metal Powder Compaction, for the Development of a Knowledge Based Powder Metallurgy Process Advisor	Bronze	Porous	1998	ABAQUS
Jinka, Lewis, Gethin	Finite Element Simulation of Powder Compaction Via the Flow Formation	Copper	Porous	1991	Unknown, Newton-Raphson Solver
Hwang, Kobayashi	Application of the Finite Element Method to Powdered Metal Compaction Processes	Copper	Porous	1991	DEFORM, Newton-Raphson Solver
Shima, Saleh	Variation of Density Distribution in Compacts in Closed-Die Compaction with Powder Characteristics	Copper	Porous	1993	Unknown
Ko, Jang, Choi, Lim, Hwang	Finite Element Method in Powdered Metal Compaction Processes	Copper	Porous	2004	DEFORM, Newton-Raphson Solver
Armstrong, Godby, Shankar Rachakonda, Cheng, McCabe	Finite Element Modelling of Cold Powder Compaction	Not defined	Granular	1993	ABAQUS

Tran *et al.* (1993), in addition to studying iron as mentioned in Section 3.1, also studied bronze, ceramics, and carbon using the Mohr-Coulomb Cap model. Armstrong *et al.* (1993) modelled a metal axisymmetric multilevel hub using the Cam-Clay model and compared single- and double-action compaction and how it affected density distributions in the component, finding that a schedule with independent motion of upper and lower punch(es) yields the highest and most uniform density distribution.

The copper powders which were investigated by several groups were all modelled using porous material models. Hwang and Kobayashi (1991) developed a porous material model to simulate the compaction of solid cylinders and rings using both single- and double-action compaction. Jinka *et al.* (1991) modelled the compaction of straight cylinders and flanged cylinders using the Shima-Oyane model in the FE simulations, and found good correlation with experimental density data. Shima and Saleh (1993) used another porous material model which had been developed by that group previously, and the aim of this study was to compare density distributions within powder compacts using copper powder particles of different shape and size. It was found that the powder shape and size did have an effect on the resulting density distributions. Ko *et al.* (2004) was co-written with Hwang, and as such used the model presented by Hwang and Kobayashi (1991) and presented the FE simulation results for several different classes of parts (Class II being represented here by a solid

cylinder and ring, Class III by a flanged cylinder, and Class IV by a multi-level cylinder) which showed results that qualitatively agree with expected results, though no experimental validation was carried out. Smith *et al.* (1998) used the Gurson porous metal plasticity model to simulate the compaction of bronze cylinders with the goal of creating an extensive database to inform designers on proper parameters for different geometries, powders, desired densities, etc. The simulated punch displacements were compared to experimental data, and were found to be very well-correlated.

3.3 Aluminum PM

In the literature, Al PM finite element models are not nearly as abundant as other metals (especially iron and copper). However, particular attention is given here as Al PM is an ever-increasing resource that PM manufacturers are currently leveraging for lightweight applications (Anderson and Foley, 2001; Huo *et al.*, 2009).

Lee and Kim (2002) used an Al6061 alloy powder in both cold isostatic pressing and die compaction tests, and used ABAQUS as their finite element code. The aim of their work was to compare several available material models to the model being proposed in their paper and how these compared to experimental data. Of the available models, it was found that the Shima-Oyane model agreed well with experimental data at the high-density region, but underestimated at the low-density region, while the Fleck-Gurson with tuned yield parameters, the Cam-clay, and the

modified Drucker-Prager Cap models slightly overestimated the density distribution of the powder compact at the low-density region, but underestimated at higher density.

3.4 Analysis of Modelling Approaches

It is interesting to note that of the twenty-two papers in the literature that were focused on the FE modelling of ferrous PM, sixteen papers used the Drucker-Prager Cap model or another granular model that incorporates a cap, such as the Cam-Clay model, and the Mohr-Coulomb Cap model, while only five papers used a porous material model, and one used an unknown material model. Figure 11 shows a breakdown of the papers that focused primarily on ferrous PM materials, and emphasizes the overwhelming tendency to use a granular material model over a porous material model.

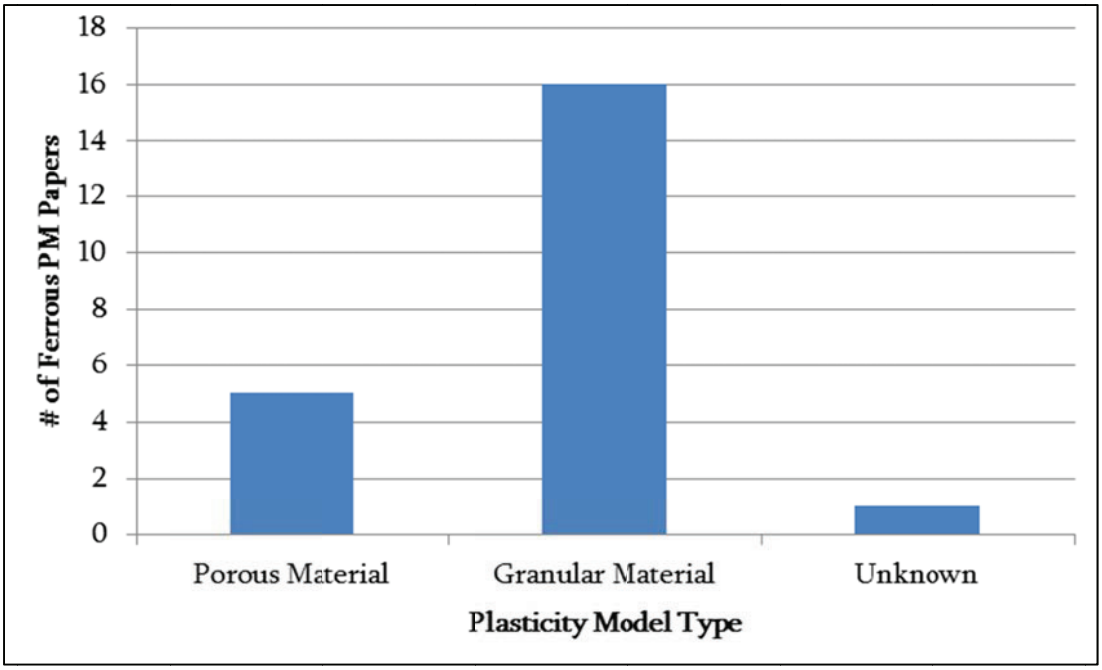

Figure 11 - Ferrous PM papers in literature by plasticity model type

It is also interesting to analyze which FE code is being utilized when a particular plasticity model type is chosen. Figure 12 incorporates all of the PM material types (ferrous and non-ferrous), and attempts to discover correlation between FE code used and plasticity model type chosen. It is shown that on average, LS-DYNA (or related codes) is used the most infrequently, regardless of plasticity model, and that ABAQUS is generally the most often used single code. It is possible that some of the unstated models could be either LS-DYNA or ABAQUS, but it was not evident from the literature papers. Ultimately, it appears that there is no general consensus on which finite element code to use based on plasticity model chosen.

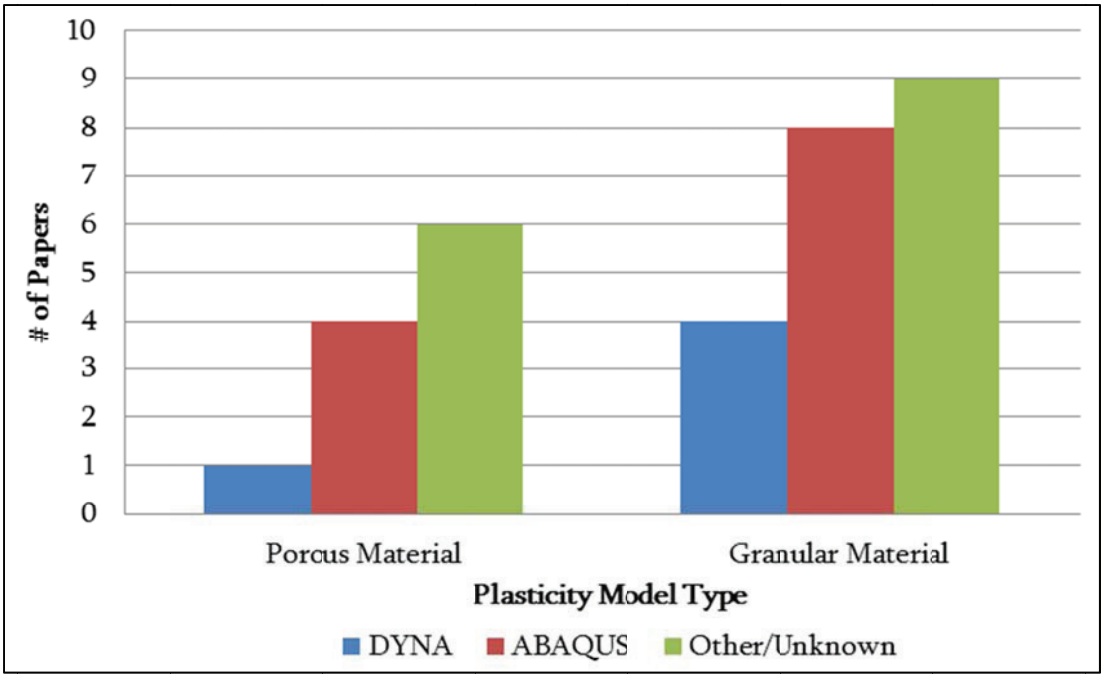

Figure 12 - Finite element code used in literature papers based on plasticity model type

3.5 Density Modelling and Validation

The density distribution within a powder compact is an important aspect within this thesis. As such, it is worthwhile to note which papers in the literature have paid close attention to this phenomenon, and more importantly, how they experimentally validated their results. This section presents the papers which have some mention of the manner in which density distribution results were validated, and discusses the feasibility of each in a university research setting.

Hehenberger (1985), Tran *et al.* (1993), and Haggblad and Oldenburg (1994) all used a technique in which the absorption of gamma rays by a layer of a powder compact is related to the density of the part. This allowed them to effectively map the density of a slice of a PM component, which could then be compared to a representative slice

from the model. However, gamma rays are expensive and a source for potential hazard for those involved in operating the machinery due to radiation.

Weber and Brown (1989) used a double correlation technique which first correlated the density between a green powder compact and an identical sintered compact, then correlated the density of the sintered part to the Rockwell hardness of the sintered part. Lee and Kim (2002) derived a similar correlation by sintering the green compacts for 20 min, which did not change the relative density of the part. The sintered parts were annealed, then tested with a Rockwell tester and a correlation equation between relative density and hardness was derived. Kim and Cho (2001), Chtourou *et al.* (2002a, 2002b) and Kang *et al.* (2007) all used variations on this hardness correlation technique to determine the density distributions throughout the powder compacts. Hardness testing requires sintering and annealing of the green compacts, as well as a determination of the correlation between hardness and density. This correlation is not readily available in the literature for the powder used in this particular research.

Krezalek and Sivakumar (1995) studied the movement of powder during compaction, and employed a technique which would allow them to see this movement experimentally. The powder was inserted into the die in layers: a thin copper layer between thick iron layers. The sample would be sintered and cut afterwards, and the deflection of each layer of powder could be seen and measured. Aydin *et al.* (1997)

used two methods to determine the density distribution within alumina compacts in this work. One, referred to as the lead-shot tracer method, has fine lead balls or a lead mesh incorporated into the powder, and x-rays are used for imaging. The second method is known as the colored layer method, where alternating layers of dyed alumina are placed in a die one after another after being very lightly compacted in order to see a sharp boundary between layers. Powder movement using lead shot tracer or powder layers gives a visual aid for displacement only, not density or strain. Introducing layers of a different powder material may also skew density measurements and powder interaction, especially when pre-compacted. The lead shot method also requires the use of x-rays which can be expensive and also a potential hazard due to radiation.

Another apparently popular method is the Archimedes method, which is to section a green compact into representative smaller sections (Coube and Riedel, 2000; Kang *et al.*, 2007), or into a fine grid pattern of much smaller cubes (Liu *et al.*, 2007) and determining the density of these individual pieces. Lee *et al.* (2008) also cut a cylinder block of a hydraulic pump made from iron powder into several sections and measured the density by water densitometry of the sintered component. Archimedes method yields a poor resolution when compared to several of the other methods, and it can also be difficult to section green compacts especially at low compaction pressures.

Chtourou *et al.* (2002a), in addition to the hardness correlation method, also used an optical densitometry technique to map the density distribution within the sample. The sample was ground and polished, and images were taken with an optical microscope. The relative density was calculated as unity minus the void ratio of the image. Ma *et al.* (2004) similarly used optical metallography to measure the density distribution in a gear made from aluminum-reinforced composite powder. Zhu *et al.* (2012) used a very simple optical densitometry example to show that, in general, there were more pores toward the bottom of a single-action sample, and fewer pores toward the top; thus, representing higher density at the top and lower density at the bottom. This method can be time consuming in preparation of the sample, and depending on the desired resolution can take a long time to capture the entire surface of the part. However, the resolution can be much finer than that of the Archimedes method.

The PM Modnet Research Group (2002) performed a very extensive study of density measuring techniques when investigating a ferrous PM component. Gamma-ray absorption, computerized tomography (CT), hardness testing, Archimedes' method (water densitometry), and optical microscopy were all used to measure the distribution found within the compact. In order to conduct the hardness testing and microscopy, the powder compacts were cut in half using a wire cutting technique as this did not load the sample, leaving its density distribution largely unchanged. The

study by the PM Modnet Group (1999) comes to the conclusion that many of the methods that they analyzed give similar results to one another.

Chapter 4: Experimental Work

In order to validate the compaction model, a number of experiments were performed on powder compacts. The experimental methods used in this thesis will be described in this chapter. These can be divided into two major categories: powder characterization and powder consolidation.

Powder characterization consists of three experiments: constructing a compaction curve, determining the apparent density of the powder prior to compaction, and determining the flow rate of the powder.

The powder consolidation category consists of powder compaction, which is the physical act of using a press to consolidate powdered metal, and optical densitometry, which is a method of mapping the density distribution within the powder compact using microscopy and photo analysis. After reviewing the available methods of density distribution analysis, it was determined that optical densitometry was the

most suitable candidate for this research, as access to a microscope and camera with imaging software is available, as are the facilities for grinding and polishing the samples to prepare them for metallography. This method provides very good resolution, though it is destructive, and preparing the samples for metallography can be time consuming.

4.1 Materials

The material used in this work is ECKA Granules Alumix 321, which is an Al6061 powder whose composition shown in Table 3. This material was used because the one paper from the literature that studied aluminum PM in depth used an Al6061 powder and having a reference with which to perform general comparison is beneficial.

Table 3 - Properties of ECKA Alumix 321 powder (ECKA Granules, 2012)

Alloy	Mg %	Si %	Cu %	Microwax C (lubricant)	Al %
AlMgSiCu	1	0.5	0.2	1.5	remainder

4.2 Powder Characterization

Several experiments have been performed to characterize the powder based on its attributes. These include creating a compaction curve based off MPIF (Metal Powder Industries Federation) Standard 45, determining the flow rate of a powder following MPIF Standard 03, and determining the apparent density of the powder following

MPIF Standard 48. The aforementioned standards were followed as closely as possible with the equipment that was available.

4.2.1 Compaction Curve

Three samples were pressed at each pressure in 100 MPa increments from 100 MPa to 500 MPa in a single-action compaction procedure in the manner described in Section 4.3.1. The material used in this powder characterization test has a lubricant premixed in the powder, so it is not necessary to add any extra lubrication during compaction. The sample heights were measured using a 0.001 mm precision micrometer. The diameter of each was measured using the same micrometer at the top, middle, and bottom of each sample, and the average of each was calculated. The samples were weighed to the nearest 0.01 g. The density of the test specimen was determined as:

$$\rho_G = 1273 \frac{m_G}{d^2 h} \tag{15}$$

where ρ_G = green density in g/cm^3, m_G = mass of test cylinder in g, d = diameter of test cylinder in mm, and h = height of test cylinder in mm. The results of the compaction curve are shown in Figure 13.

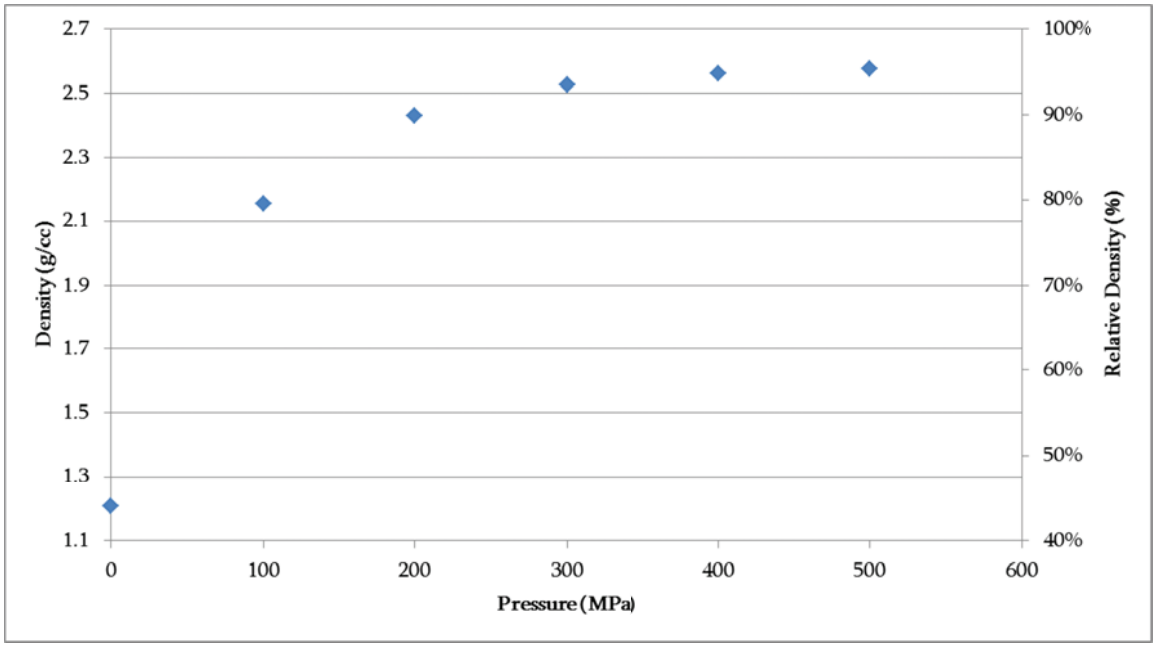

Figure 13 - Compaction curve for the means Alumix 321 using single-action compaction

The results of the compaction curve show very good repeatability at each compaction pressure, as shown in Table 4.

Table 4 - Results of compaction curve for Alumix 321 using single-action compaction

Pressure	Bulk Density (g/cc)	Relative Density (%)
0	1.207	44.7%
100	2.143	79.4%
100	2.153	79.7%
100	2.153	79.7%
200	2.432	90.1%
200	2.430	90.0%
200	2.430	90.0%
300	2.524	93.5%
300	2.528	93.6%
300	2.526	93.6%
400	2.561	94.9%
400	2.560	94.8%
400	2.561	94.8%
500	2.572	95.2%
500	2.575	95.4%
500	2.575	95.4%

4.2.2 Flow Rate Determination

This test utilizes a Hall Flowmeter Funnel (Figure 14) having a calibrated orifice of 2.54 mm diameter. As per MPIF Standard 03, the funnel is cleaned using dry paper towel and a clean dry pipe cleaner. 50.0 g of powder is measured out into a clean weighing dish. The orifice at the bottom of the funnel is blocked and the powder is carefully poured into the centre of the funnel without the powder being disturbed by tapping or moving the funnel. The emptied weighing dish is placed on the flowmeter stand directly beneath the funnel. Simultaneously, a stopwatch is started and the blockage is removed from the orifice (if the powder does not immediately start flowing, one light tap on the funnel rim may be used to get it started). The stopwatch is stopped the instant the last of the powder exits the orifice. The elapsed time is then recorded to the nearest 0.1 s.

Figure 14 - Hall flowmeter apparatus

The flow rate of this Alumix 321 powder was tested three times (18.1, 16.9, and 17.5 s/50 g) and thus the calculated average is 17.5 s/50 g.

4.2.3 Apparent Density Determination

The apparent density of powder is a parameter often used to characterize a powder. This test utilizes a cleaned test block (Figure 15) made from a hardened, tempered and demagnetized steel block with a centre hole of volume 20 cm^3 and a cleaned bushing (brass or bronze) with a diameter greater than that of the hole (see MPIF Standard 48 for exact dimensions).

Figure 15 - Arnold apparent density apparatus

A piece of cellophane or waxed paper is placed on a table, and the test block is placed upon said paper. The bushing is placed on the block, to one side of the hole. The bushing is filled slowly with powder to three-quarters of its height. With downward pressure on the bushing, the bushing is slowly slid toward the hole while also being twisted. This motion is continued until it passes the hole, at which point the bushing is brought slowly back over the hole. The sliding is slow enough that there is complete filling of the test block. The test block is removed and the pre-weighed paper is transferred to a balance and weighed to the nearest 0.1 g. The Arnold apparent density, ρ_A, is calculated as:

$$\rho_A = \frac{m_A}{V_A} = \frac{m_A}{20} \tag{16}$$

where ρ_A is the Arnold apparent density in g/cm^3, m_A is the mass of the powder in g, and V_A is the volume of the centre hole, which is 20 cm^3.

The Arnold apparent density for this Alumix 321 powder was tested three times (23.1, 23.1, and 23.1 g/20 cm^3) and thus calculated as 1.15 g/cm^3.

4.3 Powder Consolidation

4.3.1 Powder Compaction

The die compaction is carried out on an Instron universal test frame, which is a load-controlled 1 MN hydraulic press. The die used in this compaction is a simple single-action die with a diameter of 15 mm and a maximum rating of 600 MPa, a stationary lower punch located at the die-platen interface, and an upper punch which is inserted on top of the powder (as shown in Figure 16). A load cell can be inserted between the upper punch and the top platen to get a reading of the upper punch force using a portable data acquisition system.

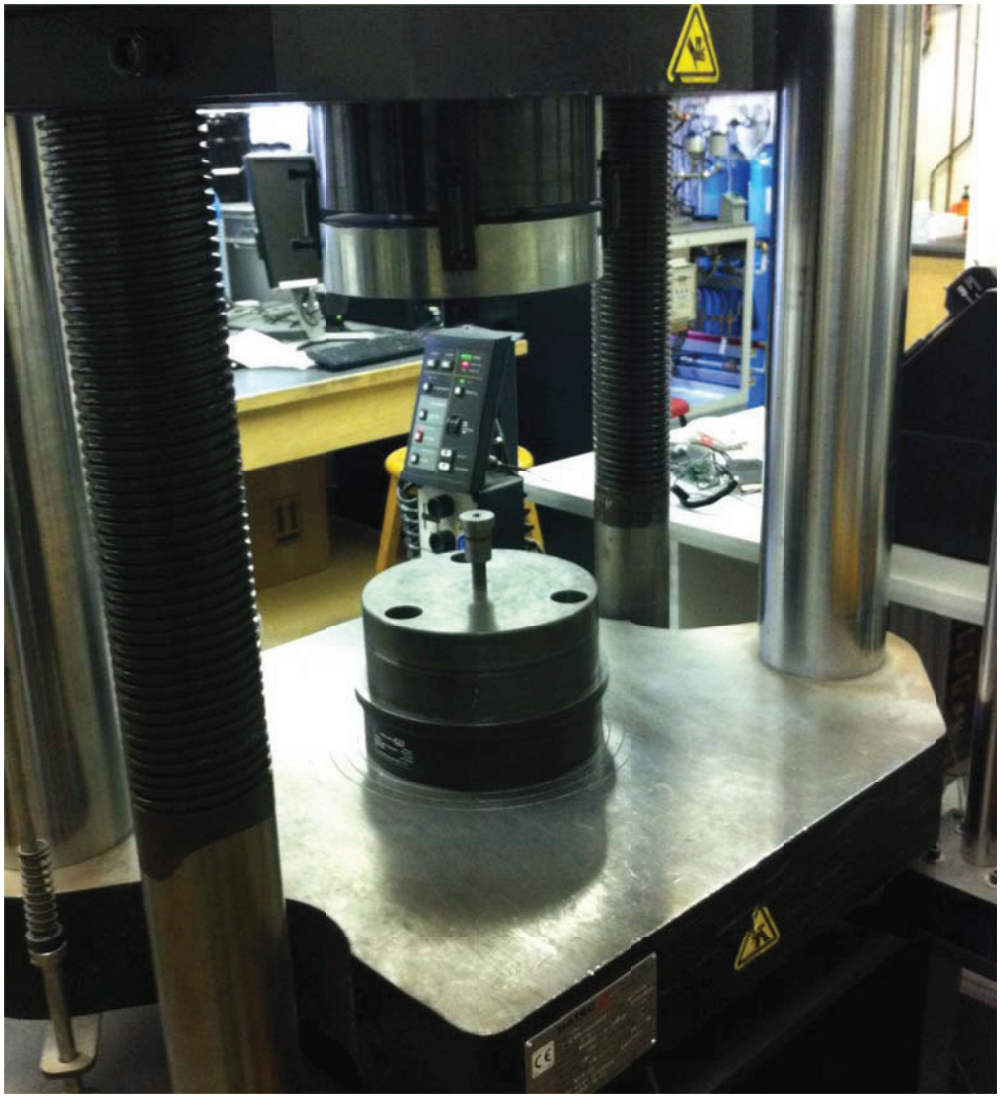

Figure 16 – Single-action die on Instron press

The experimental procedure used to produce these components is as follows:

- Weigh out 10.00 g of Alumix 321 powder
- Transfer powder to the die cavity
- Tap the die to achieve a flat surface on the top of the powder and have powder settle to approximately tap density
- Insert the upper punch and load cell

- Measure to the top of the upper punch using a height gauge
- Select the load-controller to the desired pressure
- Initiate the pressing program
- Eject the part by first removing the single-action punches, and attaching the die to a floating die apparatus which is designed to eject parts
- Place an obstruction between the die and upper platen and raise the lower platen

Three samples were pressed at each pressure for repeatability and allowing multiple tests to be performed on samples at the same compaction pressure, such as measuring bulk density or performing optical densitometry. The height of each sample before pressing was also measured so that the finite element model would have accurate initial dimensions. The height to the top of the upper punch was measured, and from this value, the height of the upper punch and lower punch were subtracted, leaving the height of the uncompacted powder column.

4.3.2 Optical Densitometry

The samples were mounted in resin, and ground to the bisecting plane of the cylinder using 240 grit sandpaper. Each sample was then ground using a 400 grit sandpaper until a relatively uniform surface with no large scratches was observed. This was followed by polishing using a 0.3 μm alumina suspension on a felt wheel for several minutes, and a solution of 0.06 μm colloidal silica on a microcloth wheel by hand for

several minutes. The polishing step of preparation for optical densitometry is not one that has a defined regimen to achieve the desired results, and as such, some of the steps above were repeated a few times to achieve a proper surface.

The analysis is performed using an Olympus BX51 optical microscope with a 5x objective lens, and a QImaging 3 megapixel digital camera equipped for data acquisition. Half of the cylinder was photographed and analyzed, as the sample is assumed to be axisymmetric and thus the two halves should be mirror images of one another.

The cylinder was mapped systematically beginning with the top outside corner. Images were collected manually by adjusting the microscope stage until the top of the image matched the bottom of the image immediately previous. An image of approximately 1.78 x 2.37 mm, with a pixel resolution of 1200 x 1600, was captured using the software package ImagePro by Media Cybernetics. Once a column was completed, the stage was reset to the top and moved sideways in the same manner as just described. At this magnification, five columns of various heights were captured, with rows of eleven samples for 100 MPa and rows of nine samples for 300 and 500 MPa. An example of this is shown in Figure 17 for the 300 and 500 MPa samples of a five column, nine row grid of images.

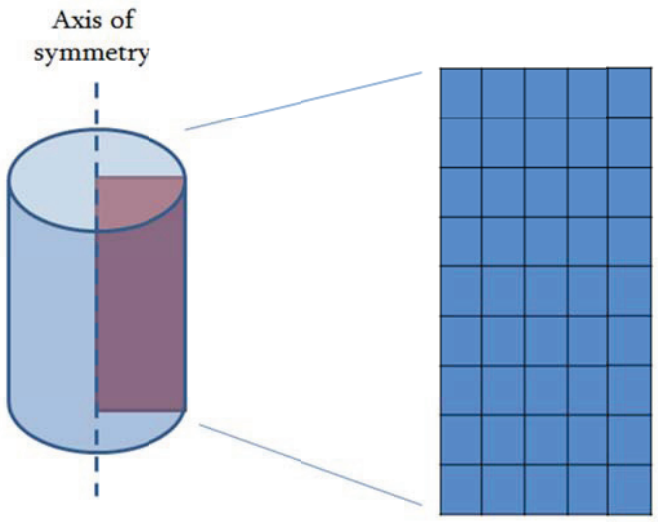

Figure 17 - Schematic of cylindrical compact and grid of images taken at 300 and 500 MPa compaction pressure

The images that are gathered are 8-bit greyscale: white representing the presence of aluminum, and black representing pores in the microstructure; an example of which is shown in Figure 18.

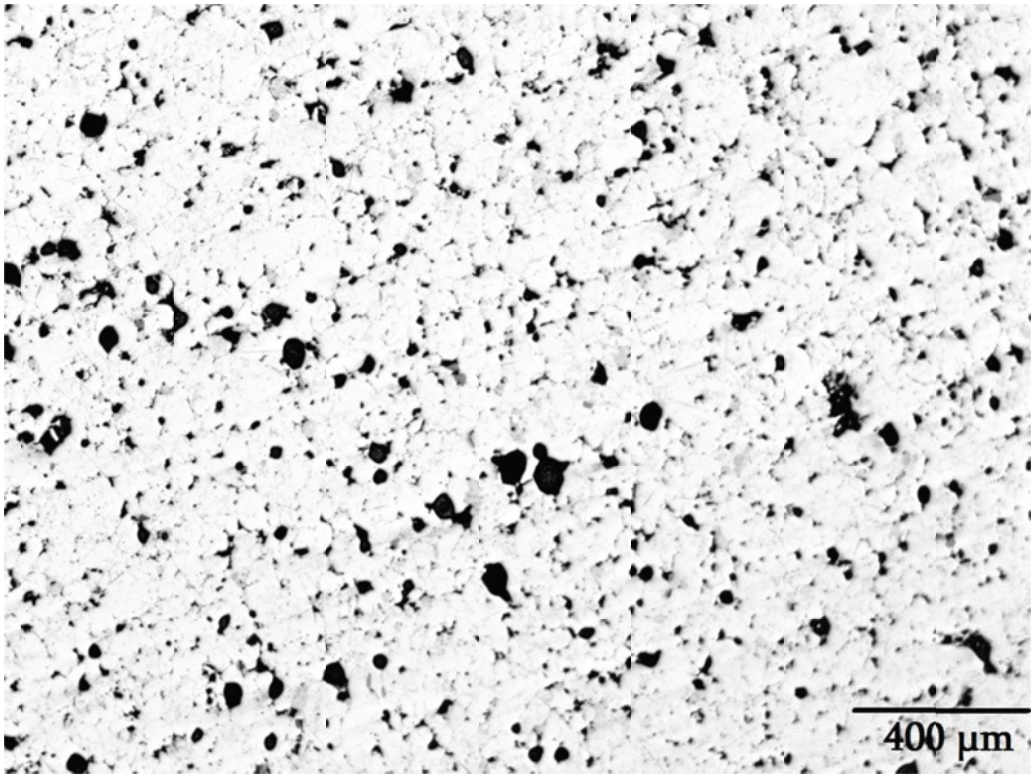

Figure 18 - Micrograph taken of 300 MPa sample (50x magnification)

The image files were then analyzed using National Instruments Vision Assistant, and the value of the percentage area that was black is returned. When this value is subtracted from 1, the result serves as a representative indication of the relative density of that specific area of the compact compared to that of fully-dense aluminum. The resulting data was processed using Microsoft Excel and MATLAB was used to display a contour map of the density distribution throughout the compact.

One variable that has a great impact on the relative density is the threshold value used by Vision Assistant for calculating the amount of black in an image. The threshold value is the number of shades of grey (this ranges from 0, which is pure black, to 255, which is pure white) that the software counts as being pure black.

Therefore, as the threshold value increases, more shades of grey get included in the count of pure black elements; this would correspond to a lower relative density calculation. For instance, Figure 19 shows an image from the 100 MPa sample analyzed once with a threshold value of 75 and once with a value of 150. The relative density of the image changes from 86.9% at the threshold of 75 to 79.6% at the threshold of 150. The threshold value is set at the value that results in the bulk density of the sample matching that of the bulk density determined by measuring the weight and geometry of the samples as in Section 4.2.1.

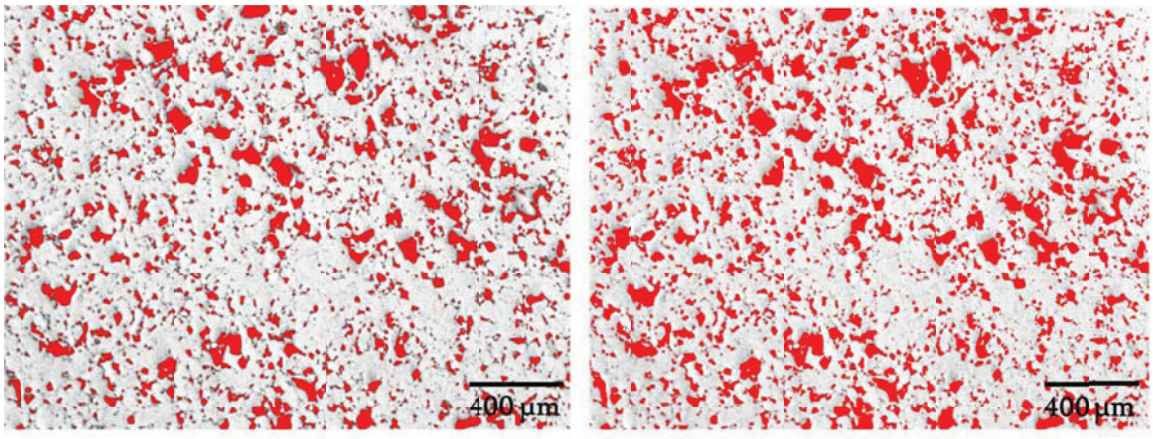

Figure 19 - Difference in bulk density with change in threshold value from 75 to 150

Furthermore, an issue can be noticed in the 100 MPa experimental sample: the outside edge of the compact appears to show damage, possibly caused by the grinding process. Figure 20 shows a micrograph from the outer edge of the sample, where damage is clearly seen.

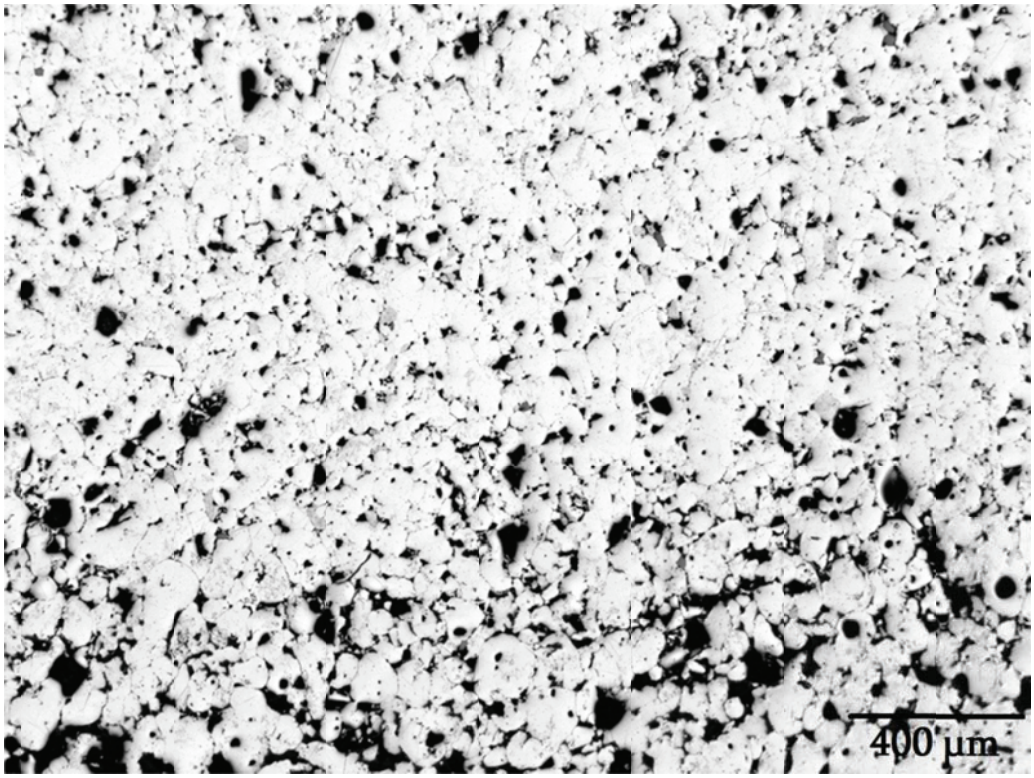

Figure 20 - Damaged edge (shown at bottom of image) of sample at 100 MPa

For analyzing the density of the images containing damaged edges (the 100 MPa sample), the damaged area was cropped out, and the density of the non-damaged portion was analyzed. The resulting value was then applied to the whole of that region. This was thought to be a satisfactory way to rectify the problem, as the overall bulk density of the sample increased by only 1-2%, resulting in a need to change the threshold level from 145 to 155 to normalize the bulk density to that of the measured bulk density from the compaction curve.

Three samples were processed in this manner: one at each of 100, 300, and 500 MPa compaction pressures. Presented in Figure 21 are the MATLAB results for the density distribution contours for the 100, 300, and 500 MPa samples, respectively.

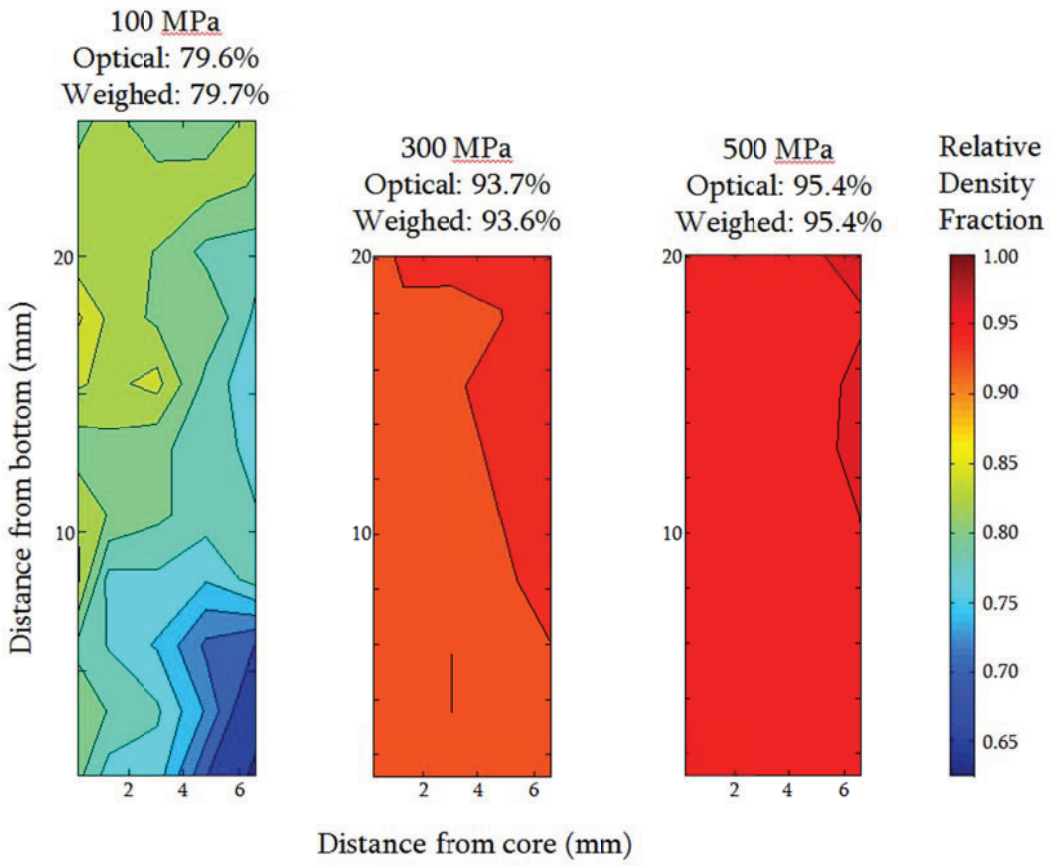

Figure 21 – Relative density contour plots for 100, 300, and 500 MPa samples using optical densitometry

The density contour maps reveal several important findings. The density contours in all three cases show a tendency to have higher density near the top half of the sample. This is where the greatest amount of powder flow is accumulating due to friction in the die wall, and where the highest density is expected to be seen. In particular, the density contour for 100 MPa shows the area of lowest density to be in the bottom outer ring, which is an expected result when comparing to the literature (German, 2005). For the 300 MPa and 500 MPa samples, the highest density is found to be in the top outside ring of the cylindrical compact, which is also a result found in the literature (German, 2005). Furthermore, it is seen that the greatest disparity between

highest and lowest density in a sample is found in the most lightly-compacted sample (85% to 63%) while the two samples compacted at higher pressure are much more uniform in density, ranging only about 2% from highest to lowest relative density.

Chapter 5: Modelling & Results

The simulations that were conducted as part of the current research are comprised of two separate models: one to simulate the powder compaction and another to simulate the elastic springback of the component after compaction. The finite element calculations are all performed using the FE hydrocode LS-DYNA version 971. The compaction and springback code used in this research can be found in Appendices A and B, respectively.

5.1 Compaction Model Description

5.1.1 Model Geometry and Mesh

A schematic of the FE powder compaction model is shown in Figure 22. The geometry of the punches, the die, and the powder were constructed and meshed into discrete elements using Altair Hyperworks 11.0. The punches and die are assumed to be rigid bodies made of steel, and the powder is modelled using axisymmetric

quadrilateral elements. The model takes advantage of the computational savings afforded by the axisymmetric formulation which is volume weighted (LS-DYNA shell formulation 15). This means that loads, among other things, are interpreted as values per unit radian (as opposed to per unit length in the area-weighted shell formulation 14) (Hallquist, 2006).

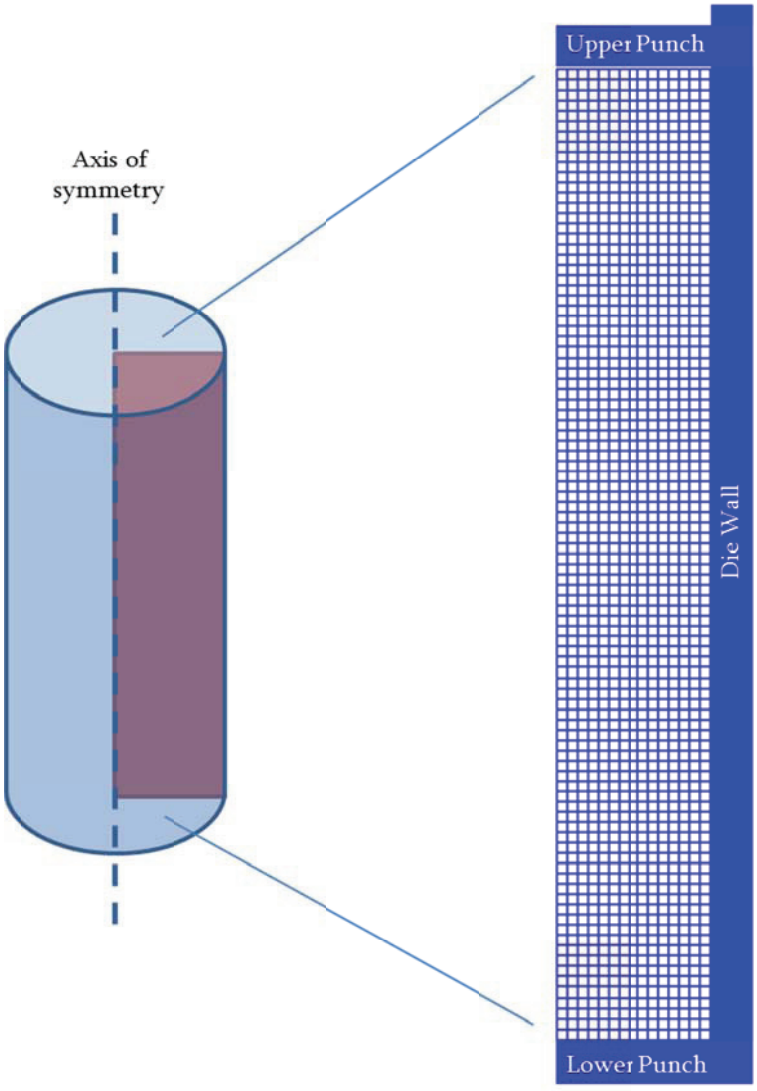

Figure 22 - Schematic of cylindrical compact and undeformed finite element simulation mesh

A mesh convergence study was conducted to determine the appropriate element size to use when modelling the powder. The model was run at 300 MPa, using single-action compaction, and the bulk density and simulation time were compared for each element size. The density contours for each element size are shown in Figure 23 to illustrate the increasing coarseness of the mesh.

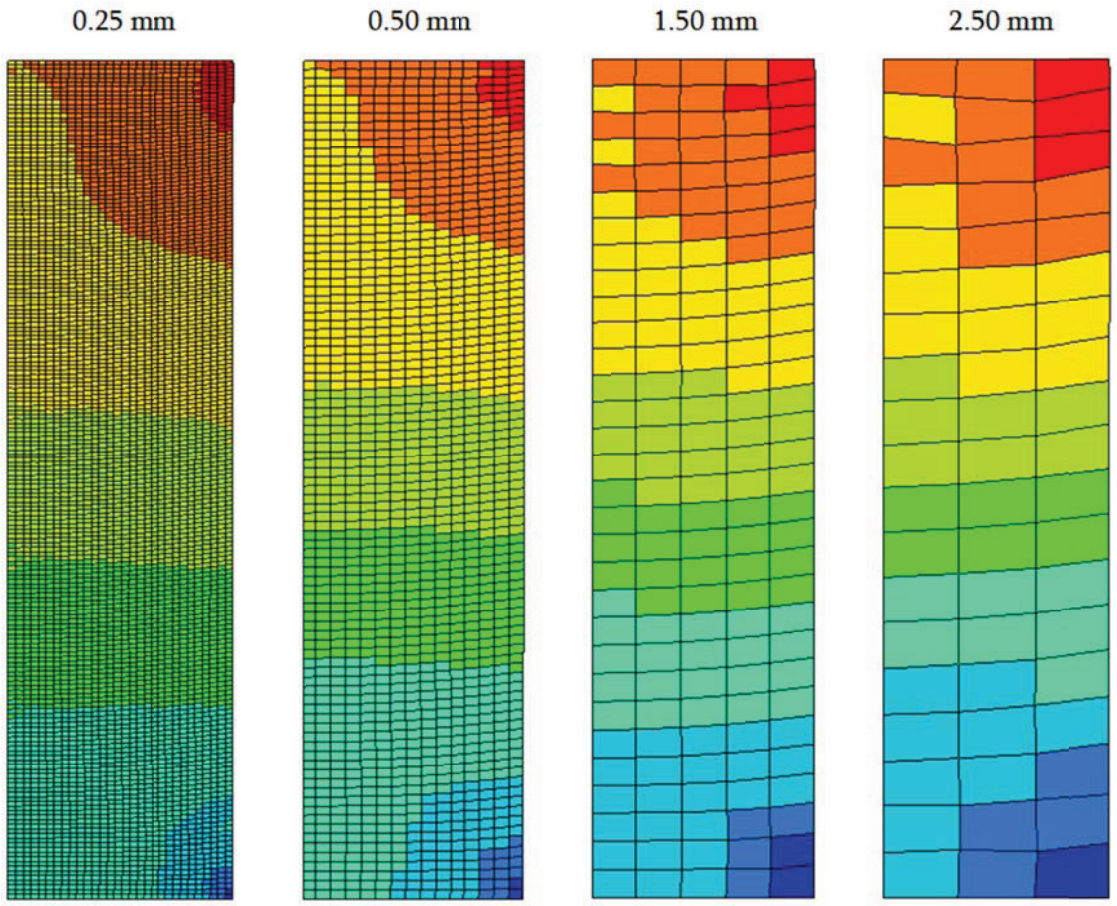

Figure 23 - Mesh convergence study - density contour maps at different element sizes (deformed mesh)

The results of the study are shown in Figure 24. The element size of 0.5 mm for the powder was selected for its stability and relatively short runtime.

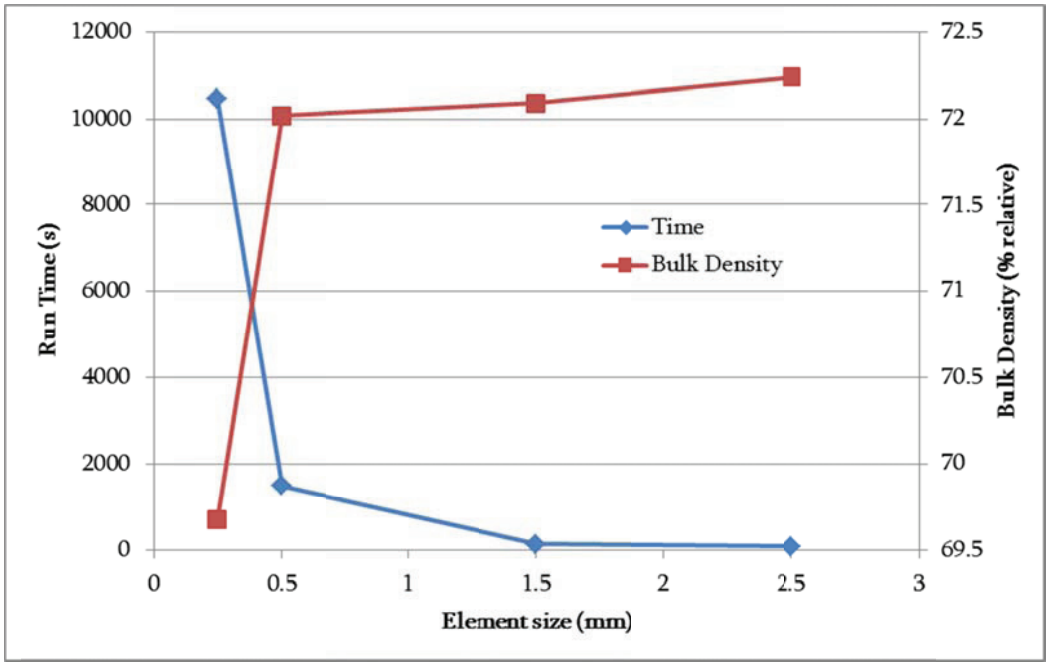

Figure 24 - Mesh convergence study – results of simulation run time and bulk density with element size

The cylindrical die has a 15 mm diameter, and the initial fill height of the powder is 46.87 mm as determined by experimental measurement, which results in the powder being represented by 1410 elements (15 columns by 94 rows).

5.1.2 Boundary Conditions and Loading

The compaction model is run using an explicit time integration and is capable of using either load or displacement control of the upper and/or lower punches. For this research, load control has been used to mimic the actual operation of the Instron press. The lower punch and die wall are both fixed in both the axial and radial directions, while the upper punch is fixed in the radial direction but free to move axially. The simulation duration is scaled down significantly, to approximately 0.1% of the original experiment duration. Simulations that normally run on the order of

the original experiment duration are often run using implicit time integration. However, the material model being used to model the powder compaction is coded to run only in explicit time integration. When a simulation of this length is run in the explicit mode, the results start to become erratic due to accumulation of error over a long period. Running at this reduced time has been shown to produce results which are consistent with literature findings (see Section 5.2), and also significantly shortens the time it takes to run the model. The contact between the die wall, punches, and powder is modelled using a surface-to-surface contact algorithm in LS-DYNA and employs a Coulomb-type friction with a value of 0.24 that was taken from the literature (Lee and Kim, 2002). Standard LS-DYNA hourglass control has been used in this model, with the default coefficient of 0.10. This is implemented to help control possible instabilities that are sometimes encountered when running models.

5.1.3 Material Model and Parameter Determination

The Alumix 321 powder was modelled using the *MAT_GEOLOGIC_CAP_MODEL keyword (Hallquist, 2006), which is a representation of the Drucker-Prager Cap model discussed in Section 2.3. The parameters used to describe the material model were derived from the experimental triaxial data presented by Lee and Kim (2002), and are presented in Table 5. The values here represent a pre-alloyed Al6061 powder supplied by Valimet used by Lee and Kim, and will be the starting point to determine

the parameters of the powder used in the experimental section of this work which is ECKA Alumix 321.

Table 5 - Compaction material model parameters for Al6061 powder from Lee and Kim (2002)

Parameter	Value
Initial density	1377 kg/m^3
Initial bulk modulus	55.76 GPa
Initial shear modulus	13.26 GPa
Failure envelope parameter, α	0 Pa
Failure envelope linear coefficient, θ	0.394
Failure envelope exponential coefficient, γ	0 Pa
Failure envelope exponent, β	0 Pa^{-1}
Cap surface axis ratio, R	2.800
Hardening law exponent, D	5E-10
Hardening law coefficient, W	0.62

5.2 Lee and Kim Validation

To validate the predicted densification of the model described in Section 5.1, a model was constructed with the geometry of the die used in Lee and Kim (2002). This die is 20 mm in diameter, and used an initial powder height of 30.05 mm. The simulation was run with the initial parameters derived from Lee and Kim's paper, and a parametric study was undertaken with the hardening law exponent, D, and the hardening law coefficient, W, to fit the model to results shown in Lee and Kim's paper. The values shown in Table 5 in Section 5.1.3 give a result that qualitatively matches the density distribution shape from the Lee and Kim DPC result (see Figure 25), with relative density values that are within 2% of those in Lee and Kim's paper;

these results have a very good correlation, given typical results (Wikman *et al.*, 2006; Khoei *et al.*, 2006) in the literature.

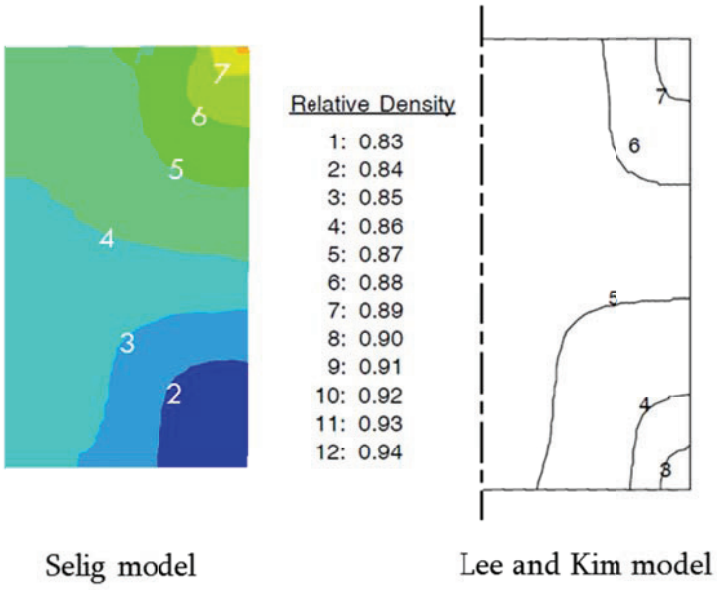

Figure 25 - Comparison of density distributions in Selig model and Lee and Kim model (2002)

These parameters will be used as a starting point for the determination of the model parameters for the Alumix 321 powder.

5.3 Compaction Model Results

The compaction model was run with pressures in 100 MPa increments from 100 - 500 MPa. Two main results will be discussed: the compaction curve generated from the bulk density of the compacts, and the density distribution found within a compact.

5.3.1 Simulated Compaction Curve Results and Comparison

In order to develop appropriate parameters for the Alumix 321 powder, the simulation results were compared to the experimental work conducted in Section

4.2.1. The initial relative density of the Alumix 321 powder in the die was calculated using the height of the powder column in the die, and the initial bulk and shear modulus were estimated to be those values corresponding to fully-dense Al6061 multiplied by the initial relative density. A parametric study with the D and W parameters was conducted to attempt to match the bulk density of the finite element sample at each compaction pressure to the experimental samples. LS-DYNA calculates the effective plastic strain within each element, which is then converted to relative density through the relationship derived from Coube and Riedel (2000).

$$\varepsilon_v^p = \ln\left(\frac{V}{V_0}\right) = \ln\left(\frac{\rho_{rel,f}}{\rho_{rel,0}}\right) \tag{17}$$

The bulk density was calculated by averaging the effective plastic strain over all the elements in the powder, and converting it to relative density, where the resulting compaction curve is shown in Figure 26.

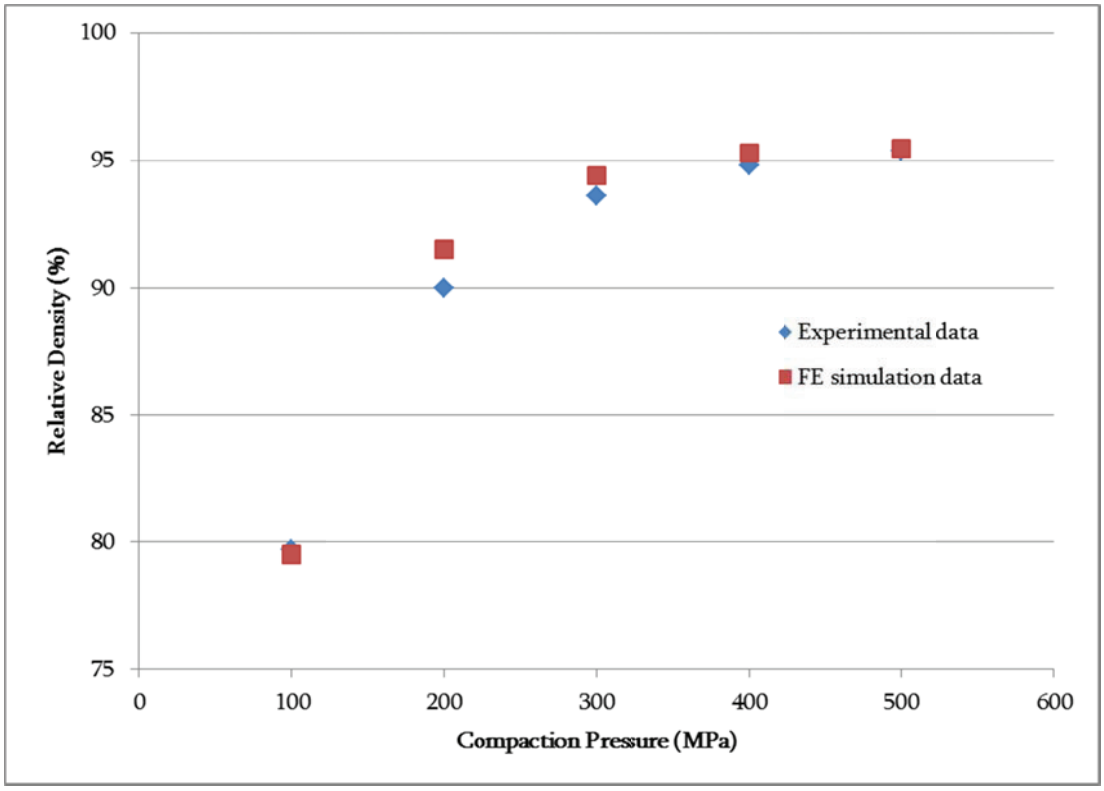

Figure 26 - Comparison of relative bulk density from FE simulation to experimental compaction curve data

The resulting compaction curve using these parameters shows an excellent correlation between simulation data and experiment at the lowest compaction pressure, 100 MPa, and at the highest compaction pressure, 500 MPa, within 0.2% relative density. The values in between are slightly overestimated using the finite element simulation, but are considered a very good match. In the absence of a triaxial testing apparatus, it has been shown in this research that fitting the parameters by matching the compaction curves generated by physical experiment and finite element simulation is a suitable substitute. The DPC parameters are shown in Table 6.

Table 6 - Final compaction material model parameters for Alumix 321 powder

Parameter	Value
Initial density	1207 kg/m^3
Initial bulk modulus	48.87 GPa
Initial shear modulus	11.62 GPa
Failure envelope parameter, α	0 Pa
Failure envelope linear coefficient, θ	0.394
Failure envelope exponential coefficient, γ	0 Pa
Failure envelope exponent, β	0 Pa^{-1}
Cap surface axis ratio, R	2.800
Hardening law exponent, D	1.4E-9
Hardening law coefficient, W	0.76

5.3.2 Simulated Density Distribution Results and Comparison

The density distribution within powder compacts at each pressure was investigated. As mentioned in Section 5.3.1, LS-DYNA calculates the effective plastic strain for each element; this value is then converted into percent relative density.

Figure 27 shows the deformed sample and the density distribution within the compact at 100, 300, and 500 MPa.

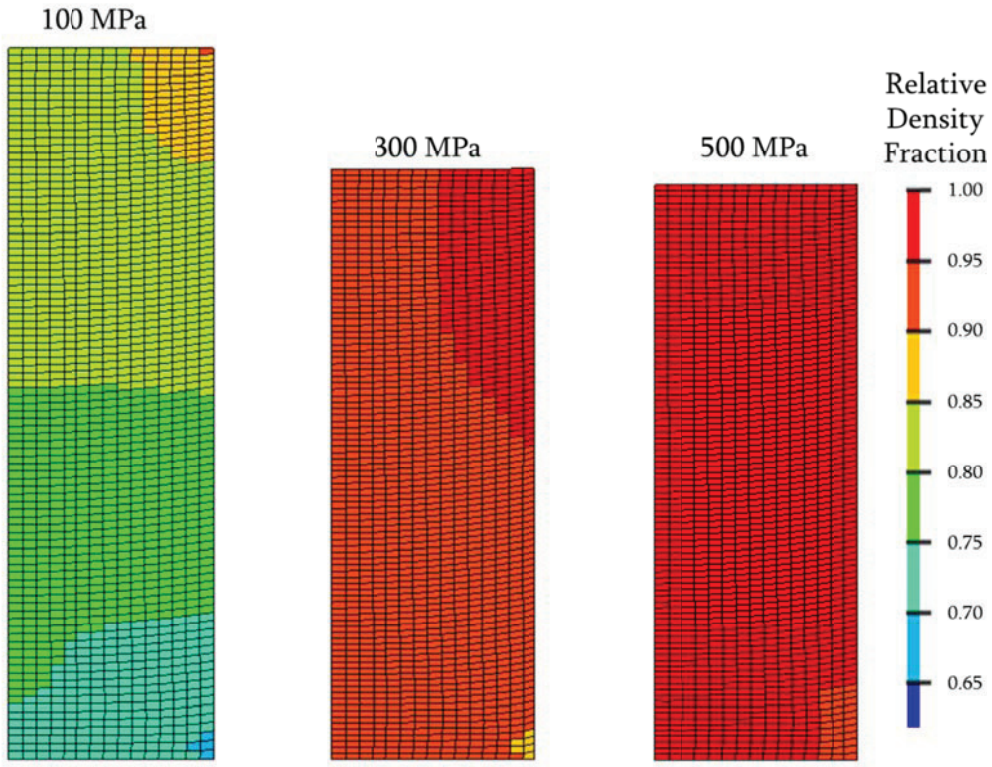

Figure 27 - Relative density distribution within powder compact at 100, 300 and 500 MPa using the FE model

For the 100 MPa sample, the element with the highest density is 90.4% and lowest is 67.0%. For the 300 MPa sample, the highest density is 95.6% and lowest is 86.1%. For the 500 MPa sample, the highest density is 95.6% and lowest is 90.6%. In all cases, the density distribution qualitatively agrees with the predicted trend for density contours in a single-action die compaction (German, 2005), where the highest density occurs in the top outer ring of the powder compact, while the lowest density occurs in the bottom outer ring.

Furthermore, the difference between the highest density and lowest density is greatest when the compaction pressure is low (23.4% difference at 100 MPa), and this

difference becomes very small as compaction pressure is increased (5% difference at 500 MPa).

The information that can be extracted from the optical densitometry density distribution contour maps can be directly compared to the information taken from those created from the FE simulations. Figure 28, Figure 29, and Figure 30 show the density distributions for 100, 300, and 500 MPa, respectively, for the optical densitometry experiments and the FE simulations. Since the threshold value for the optical densitometry analysis was set so that the bulk density matched that of the physical compaction curve data, the contours can be compared directly between the densitometry and FE simulation data. The apparent size difference in the images is attributed to the fact that the optical densitometry contour maps are bound by the centroids of the outermost data points, which trims approximately 1 mm off the external borders. Furthermore, the FE simulation results have been flipped about the vertical axis to show a "mirror-image" comparison with the optical densitometry results.

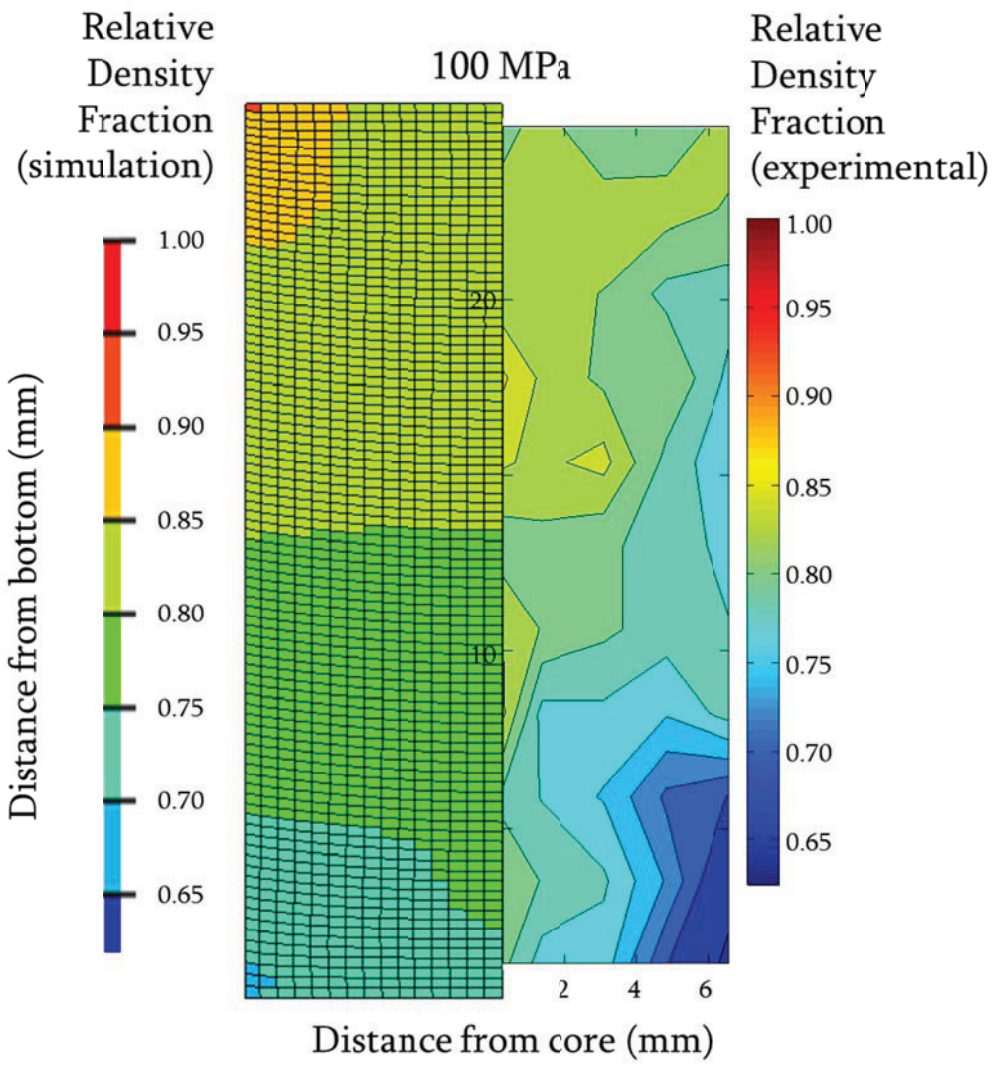

Figure 28 - Comparison of density contour maps from experiment and finite element simulation (100 MPa)

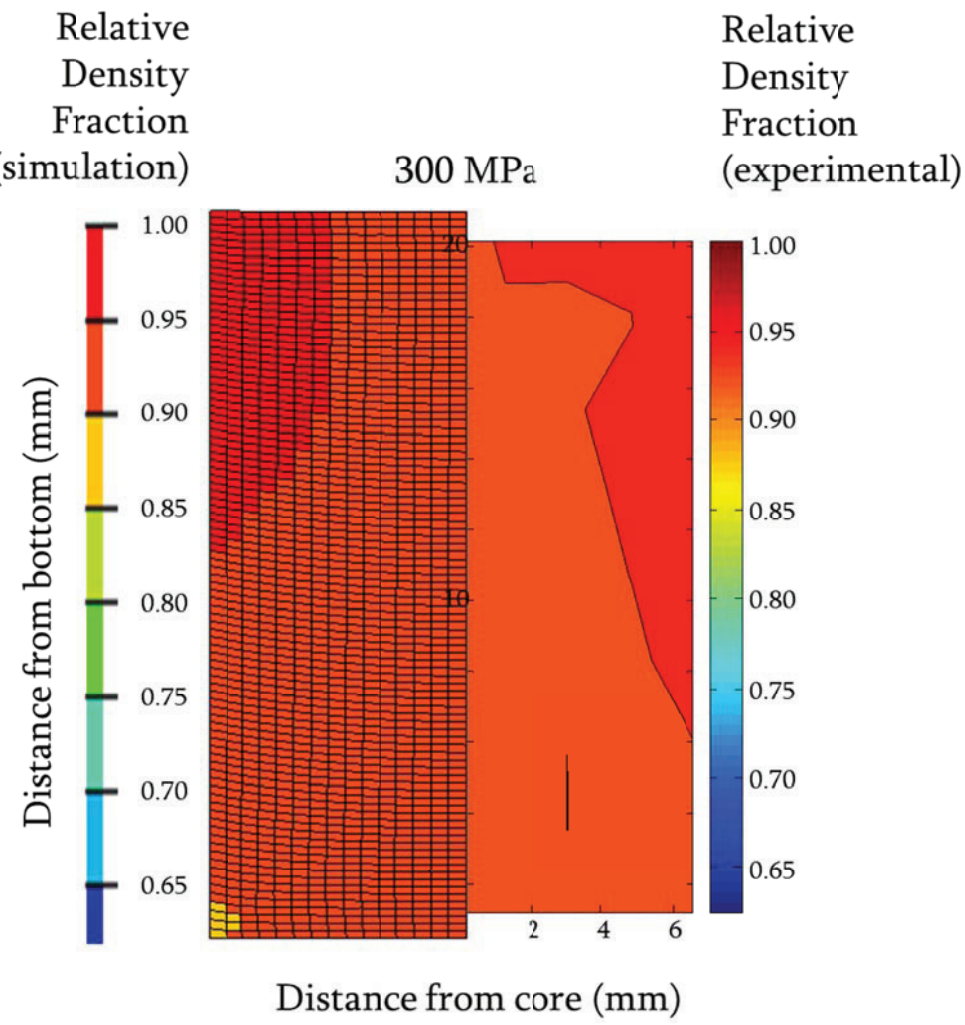

Figure 29 - Comparison of density contour maps from experiment and finite element simulation (300 MPa)

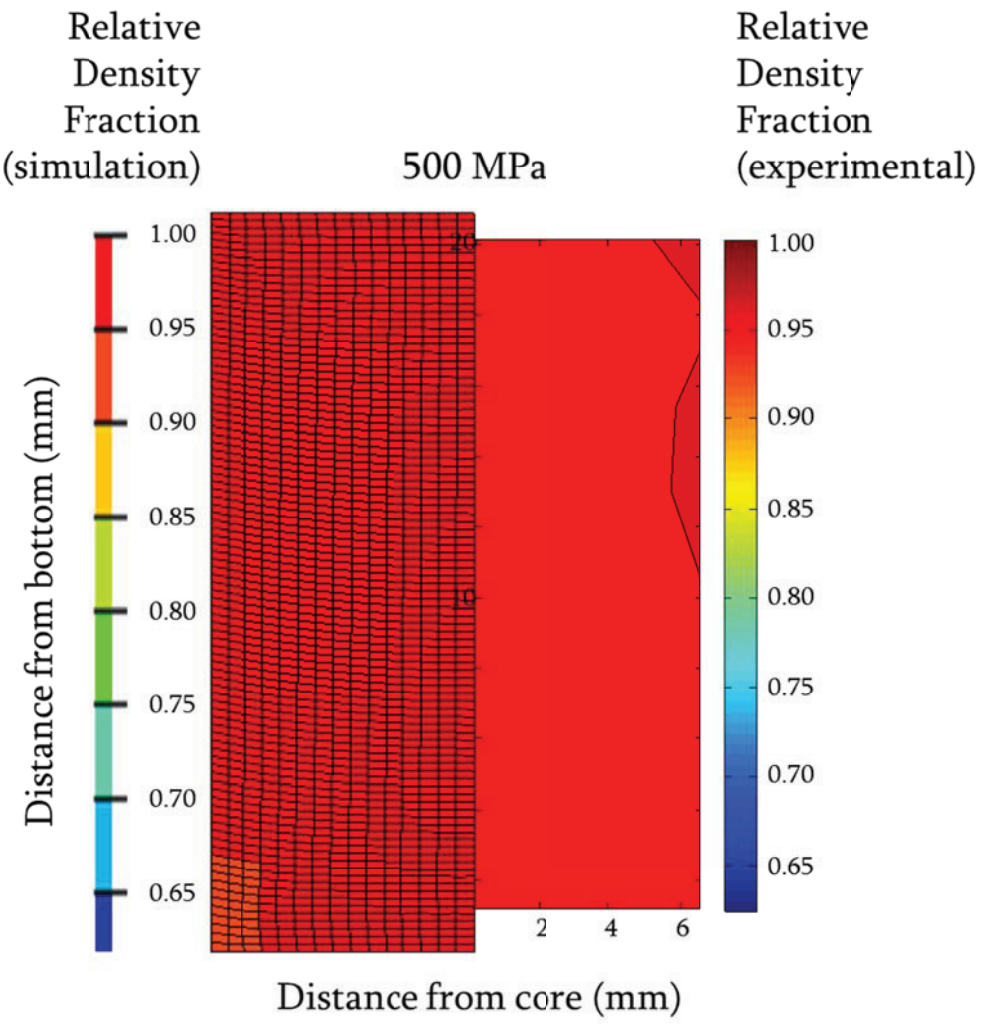

Figure 30 - Comparison of density contour maps from experiment and finite element simulation (500 MPa)

Though the contours are not identical, the trends found between the densitometry and finite element simulations are qualitatively very similar. The greatest difference between high and low density regions in a single compact is shown to be in the 100 MPa case in both the experimental data and simulation, and the uniformity in density increases as the compaction pressure is increased in both cases. In both instances as well, the highest density region is toward the top of the sample, whereas the lowest density region is toward the bottom of the sample.

From this data, it shows that the two methods of analyzing the density contours in an Alumix 321 green sample are similar to one another, and acceptable representations of this information.

5.4 Springback Model

Once the compaction model has reached completion, LS-DYNA writes a file which stores the final state of stress of the model and effective plastic strain that has occurred during compaction. This file is then read into another simulation that models springback of the compact. The springback model runs using the LS-DYNA implicit code, as opposed to the explicit code used to model compaction. The state of stress of each element is initialized in the solver, and the solver uses this as the input to calculate the eventual equilibrium of the system after elastic springback has taken place.

As springback is essentially the release of elastic strain in the model, the DPC model is replaced by an elastic constitutive material model for this simulation. The density used for the springback model is the final density of the compaction simulation, and the elastic modulus for the model is approximated as being the value of fully-dense Al6061 multiplied by the relative density (Ma *et al.*, 2004) and Poisson's ratio is assumed to be $\nu = 0.30$.

5.5 Springback Model Results

The springback of the model at 100, 300, and 500 MPa was determined from the elastic springback model. Figure 31 shows a contour plot of radial displacement of the equilibrated compact after the springback simulation takes place for compaction pressures of 100, 300, and 500 MPa.

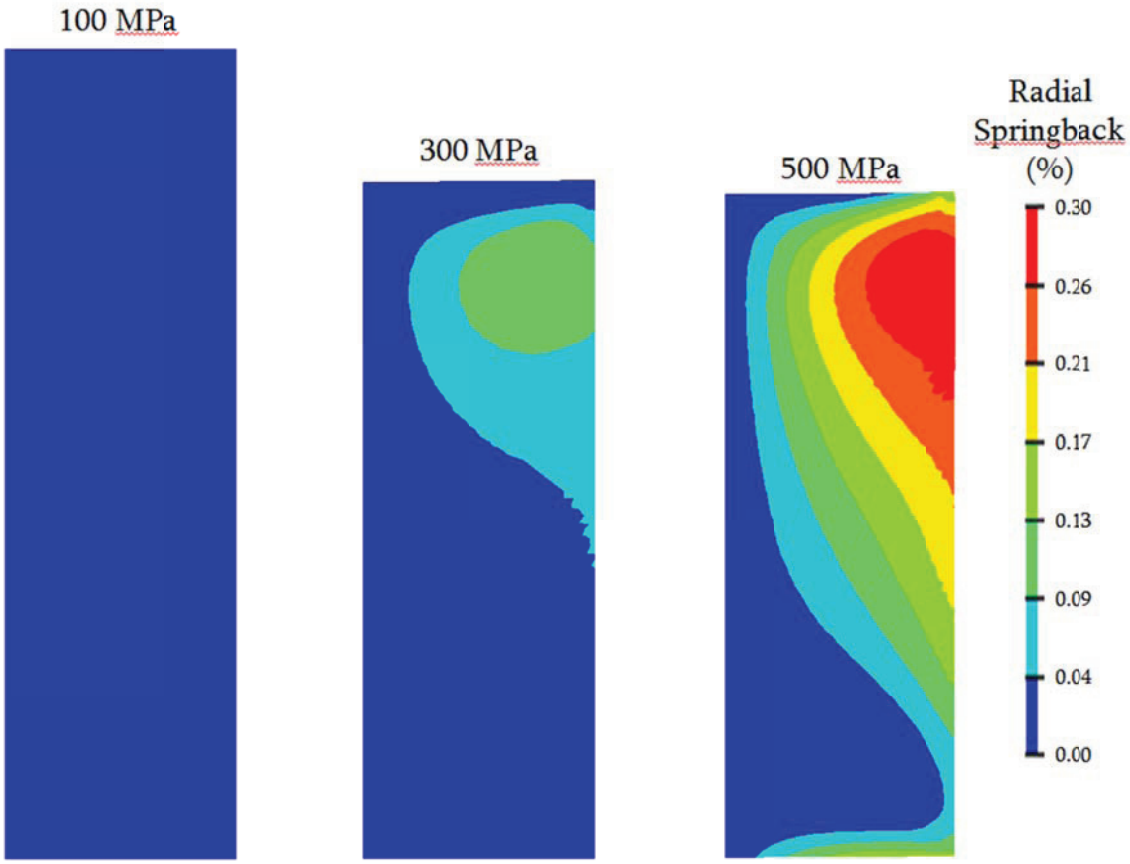

Figure 31 - Radial springback of compact at 100, 300, and 500 MPa from finite element simulation

The fringe values in Figure 31 illustrate several of the fundamental mechanics of springback. The radial displacement values are very close to zero along the core, and the compact experiences an overall radial expansion; both of these responses are to be

expected. Warping of the compact is apparent: a non-constant densification should lead to differing amounts of springback, as density is related to strength, which is related to residual stress, which ultimately controls springback.

Evaluating the percent dimensional change at several points along the height of the compact shows that the dimensional change is closely related to the relative bulk density at each area within the compact. Figure 32 illustrates the values of radial springback at 3 locations (25%, 50%, and 75% from the top of the compact) for three compaction pressures. The springback increases with both compaction pressure and local bulk density. These values are on the same order of the springback experienced by compacts upon ejection from a die when compared to values from a study conducted on a prealloyed aluminum composite by Ma *et al.* (2004) and also German (2005), who states that a typical value is from 0.2 - 0.4%.

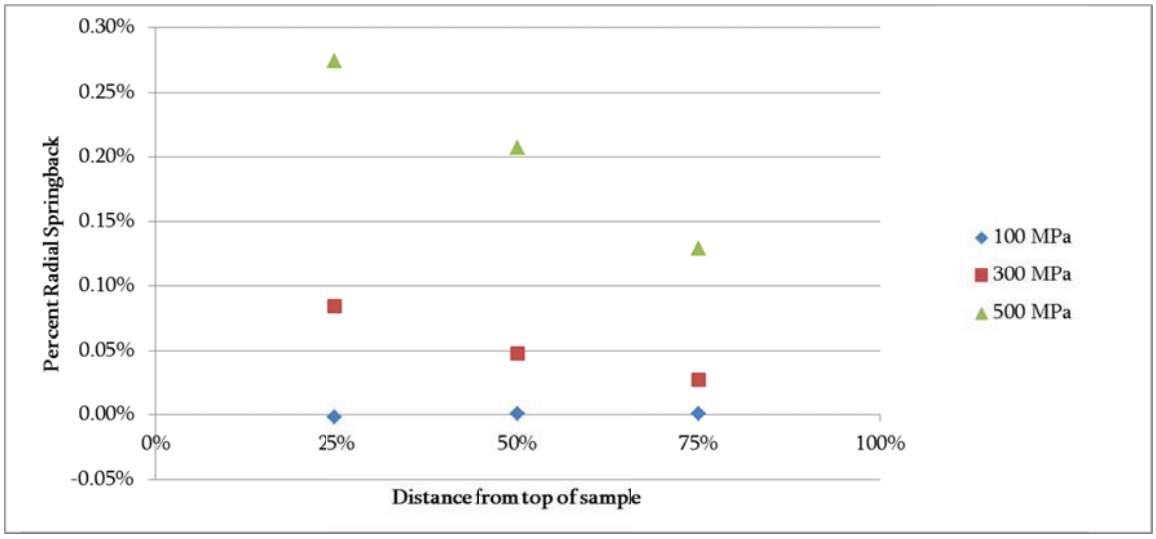

Figure 32 - Percent radial springback along height of compact from finite element simulation

The diameters of the PM green compacts at each compaction pressure were measured at the top, middle, and bottom of the sample. These were converted into percent radial expansion, and graphed in Figure 33 alongside the percent radial expansion calculated from the FE springback model.

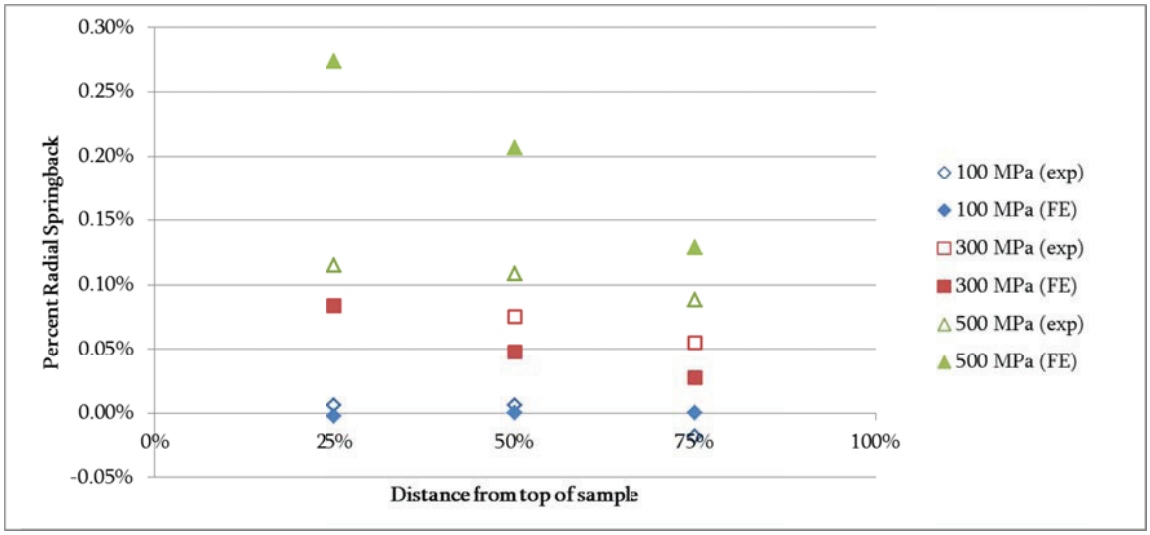

Figure 33 - Comparison of radial springback from experimental measurements and finite element simulation

From this comparison, it is evident that both the experiment and FE simulation show similar trends: the radial springback decreases from the top of the sample to the bottom of the sample, and the radial springback increases overall with increasing compaction pressure. The results for both methods at 100 and 300 MPa show results that are very comparable with one another. The results at 500 MPa show larger springback in the simulation when compared to the experimental measurements, and this difference is much more evident near the top of the sample. It is thought that this could be attributed to the way in which the springback process is currently

modelled: a compact being ejected slowly from a die after compaction at high pressure could result in smaller springback values near the top of the compact as this is the first part of the compact to be free of the die, and therefore is restricted from expanding as much as it would in an unrestricted case. However, the current springback process being modelled is a simple relaxation of the compact where the springback is experienced at all heights simultaneously.

Chapter 6: Conclusions & Recommendations

This research contributed several important findings in finite element simulation of Alumix 321 PM. A thorough background detailing the powder compaction process and factors that influence it was given. A literature review was conducted which classified powder compaction papers by powder type, material model, and finite element code used. This classification can be used by future powder researchers to help determine which route to follow to model a particular type of powder.

A new finite element model has been developed for Alumix 321 PM to predict the density within green compacts over a wide range of compaction pressures in single-action compaction. The powder parameters were originally taken from the literature for a similar powder, but were altered for the powder in this work by conducting a parametric study and fitting the resulting bulk densities of the samples to the experimental compaction curve. This was deemed to be a good substitute when

access to a triaxial compaction apparatus is not available. This model can also predict the springback of a green compact to a good degree of accuracy when compared to experimental results, at compaction pressures of 300 MPa or less.

Optical densitometry was shown to be an effective method for experimentally determining the density gradients within a powder compact with a very good resolution.

Recommendations for future work include:

- As new papers get added to the literature, it is recommended that the tables which are included in the literature review should continue to be updated by the research group.
- The model has the capability to have the upper punch and lower punch actuate, so a recommendation for the next step for the model would be to experimentally validate the model when using double-action compaction, or the floating die apparatus used often in research settings which simulates double-action compaction on a single-action press.
- The springback model should be modelled with a full ejection schedule to study the effects of the release from the die on overall dimensional change, especially at high pressures.
- A recommendation to increase the quality of the polished samples would be to mitigate the damage caused around the external edges of the compact at low

pressures by testing different polishing methods to determine how much of an effect the grinding and polishing has on the sample edges. This would minimize the amount of image manipulation necessary to extract the information for the density contour maps.

- A study should be done on the repeatability of the optical densitometry method, as well as a sensitivity analysis of the effect of magnification on density contour maps.

References

Anderson, I. E., Foley, J. C. (2001). Determining the role of surfaces and interfaces in the powder metallurgy processing of aluminum alloy powders. *Surface and Interface Analysis*, 31, 599-608.

Armstrong, S., Godby, V., Shankar Rachakonda, V. B., Cheng, S., McCabe, T. J. (1993). Finite element modelling of cold powder compaction. *Proceedings of the 1993 International Conference & Exhibition on Powder Metallurgy & Particulate Materials, 3, Modeling, design, and computational methods*, 165-73.

Aydin, I., Briscoe, B. J., Ozkan, N. (1997). Modelling of powder compaction: A review. *MRS Bulletin*, 22(12), 45-51.

Ball, W. G., Hinger, F. W., McKotch, R. A., Pfingstler, H. D., Phillips, R. R. (1995). Replacing internal with external lubricants: Phase II. *Advances in Powder Metallurgy and Particulate Materials*, 1(2), 2/11-2/23.

Brown, J. D., Castle, G. S. P., Chagnon, F., Inculet, I. I., (1999). Electrostatic lubrication of molds. *IEEE Transactions on Industry Applications*, 35(1), 213-7.

Calero, J. A. (2006). PM Modelling: overview and industry standpoint. *Powder Metallurgy*, 49(1), 10-2.

Chtourou, H., Guillot, M., Gakwaya, A. (2002a). Modeling of the metal powder compaction process using the cap model. Part I. Experimental material characterization and validation. *International Journal of Solids and Structures*, 39(4), 1059-75.

Chtourou, H., Guillot, M., Gakwaya, A. (2002b). Modeling of the metal powder compaction process using the cap model. Part II. Numerical implementation and practical applications. *International Journal of Solids and Structures*, 39(4), 1077-96.

Cocks, A. C. F. (2001). Constitutive modelling of powder compaction and sintering. *Progress in Materials Science*, 46, 201-29.

Coube, O., Cocks, A. C. F., Wu, C.-Y. (2005). Experimental and numerical study of die filling, powder transfer and die compaction. *Powder Metallurgy*, 48(1), 68-76.

Coube, O., Riedel, H. (2000). Numerical simulation of metal powder die compaction with special consideration of cracking. *Powder Metallurgy*, 43(2), 123-31.

Coulomb, C. A. (1776). Essai sur une application des regles des maximis et minimis a quelquels problemes de statique relatifs, a la architecture, *Mem. Acad. Roy. Div. Sav.*, **7**, 343-87.

Cunningham, J. C., Sinka, I. C., Zavaliangos, A. (2004). Analysis of Tablet Compaction. I. Characterization of Mechanical Behavior of Powder and Powder/Tooling Friction. *Journal of Pharmaceutical Sciences*, 93, 2022-39.

Doremus, P., Geindreau, C., Martin, A., Debove, L., Lecot, R., Dao, M. (1995). High pressure triaxial cell for metal powder. *Powder Metallurgy*, 38(4), 284-7.

Doremus, P., Toussaint, F., Alvain, O. (2001). Simple tests and standard procedure for the characterisation of green compacted powder. *Recent Developments in Computer Modelling of Powder Metallurgy Processes*, 29-41.

Drucker, D. C., Prager, W. (1952). Soil mechanics and plastic analysis on limit design. *Quarterly of Applied Mathematics*, 10, 157-65.

ECKA Granules. (2012). ECKA Alumix Typical Chemical Composition, Physical Characteristics, and Sintered Properties. URL: http://www.ecka-granules.com/index.php?id=153&typ=15&anwendung=3&L=2.

Fleck, N. A., Kuhn, L. T., McMeeking, R. M. (1992). Yielding of metal powder bonded by isolated contacts. *Journal of the Mechanics and Physics of Solids*, 40(5), 1139-62.

German, R.M. (1994). *Powder Metallurgy Science.* (2nd ed.). Princeton, NJ: Metal Powder Industries Federation.

German, R. M. (2005). *Powder Metallurgy & Particulate Materials Processing*. Princeton, NJ: Metal Powder Industries Federation.

Gurson, A. L. (1977). Continuum theory of ductile rupture by void nucleation and growth. I. Yield criteria and flow rules for porous ductile media. *Transactions of the ASME. Series H, Journal of Engineering Materials and Technology*, 99(1), 2-15.

Haggblad, H., Oldenburg, M. (1994). Modelling and simulation of metal powder die pressing with use of explicit time integration. *Modelling and Simulation in Materials Science and Engineering*, 2(4), 893-911.

Hallquist, J. (2006). *LS-DYNA Theory manual*. Livermore, California: Livermore Software Technology Corporation.

Hehenberger, M. (1985). Computer aided engineering in product development of PM parts: Finite element simulation of die compaction. *Proceedings of the 1984 International Powder Metallurgy Conference*, 679-97.

Huo, S., Heath, B., Ryan, D. (2009). Applications of powder metallurgy aluminums for automotive valve-trains. *SAE International Journal of Materials and Manufacturing*, 1(1), 511-15.

Hwang, B., Kobayashi, S. (1991). Application of the finite element method to powdered metal compaction processes. *International Journal of Machine Tools Manufacture*, 31(1), 123-37.

Jinka, A. G., Lewis, R. W., Gethin, D. T. (1991). Finite element simulation of powder compaction via the flow formulation. *Advances in Powder Metallurgy, 1, Compaction, Quality Control and Training*, Chicago, Illinois, USA, 123-44.

Kang, C. S., Lee, S. C., Kim, K. T., Rozenberg, O. (2007). Densification behavior of iron powder during cold stepped compaction. *Materials Science and Engineering A*, 452-453, 359-66.

Khoei, A. R. (2005). Powder constitutive models. *Computational Plasticity in Powder Forming Processes*, 44-100. Cornwall: Elsevier.

Khoei, A. R., Azami, A. R., Azizi, S. (2007). Computational modelling of 3D powder compaction processes. *Journal of Materials Processing Technology*, 185(1-3), 166-172.

Khoei, A. R., Shamloo, A., Azami, A. R.. (2006). Extended finite element method in plasticity forming of powder compaction with contact friction. *International Journal of Solids and Structures*, 43(18-19), 5421-48.

Kim, K. T., Cho, J. H. (2001). A densification model for mixed metal powder under cold compaction. *International Journal of Mechanical Sciences*, 43, 2929-46.

Ko, B. D., Jang, D. H., Choi, H. J., Lim, J. Y., Hwang, B. (2004). Finite element method in powdered metal compaction processes. *Materials Science Forum*, 449, 109-12.

Korachkin, D., Gethin, D. T., Lewis, R. W., Tweed, J. H., Guyoncourt, D. M. M. (2008). Measurement of Young's modulus and tensile failure properties of green powder compacts. *Powder Metallurgy*, 51(2), 150-9.

Krezalek, I., Sivakumar, K. (1995).Computational simulation of powder movement during uni-axial die compaction of metal powders. *Journal of Materials Processing Technology*, 48(1), 421-7.

Kuhn, H. A., Downey, C. L. (1971). Deformation characteristics and plasticity theory of sintered powder materials. *International Journal of Powder Metallurgy*, 7(1), 15-25.

Lee, M. C., Chung, S. H., Cho, J. H., Chung, S. T., Kwon, Y. S., Kim, H. J., *et al.* (2008). Three-dimensional finite element analysis of powder compaction process for forming cylinder block of hydraulic pump. *Powder Metallurgy*, 51(1), 89-94.

Lee, S. C., Kim, K. T. (2002). Densification behavior of aluminum alloy powder under cold compaction. *International Journal of Mechanical Sciences*, 44(7), 1295-1308.

Li, Y. Y., Ngai, T. L., Zhang, D. T., Long, Y., Xia, W. (2002). Effect of die wall lubrication on warm compaction powder metallurgy. *Journal of Materials Processing Technology*, 129, 354-8.

Liu, M., Xia, W., Zhou, Z., Li, Y. (2007). Numerical simulation of metal powder compaction considering material & geometrical nonlinearity. *2007 IEEE International Conference on Control and Automation*, 908-12.

Livermore Software Technology Corporation. (2007). *LS-DYNA Keyword User's Manual*, *Volume 1*, California: LSTC.

Ma, L., Zahrah, T., Fields, R. (2004). Numerical three dimensional simulation of cold compaction and springback for prealloyed powder composites. *Powder Metallurgy*, 47(1), 31-6.

MACE3 Lab, Laval University. (2012). http://mace3.fsg.ulaval.ca/en/recherche/equipements/etc.

Menzies, B. K. (1988). A Computer Controlled Hydraulic Triaxial Testing System. *Advanced Triaxial Testing of Soil and Rock, ASTM STP 977, American Society for Testing and Materials*, Philadelphia, 82-94.

Mikhailov, O. V., Shtern, M. B. (2003). Numerical modelling of the compaction of powder articles of complex shape in rigid dies: effect of compaction scheme on density distribution II. Modelling procedure and analysis of forming schemes. *Powder Metallurgy and Metal Ceramics*, 42(3-4), 114-21.

Ngai, T. L., Chen, W., Xian, Z., Wen, L., Wu, Y. (2002). Die wall lubricated warm compaction of iron-based powder metallurgy metal. *Transactions of Nonferrous Metals Society of China*, 12(6), 1095-8.

Oyane, M., Shima, S., Kono, Y. (1973). Theory of plasticity for porous metals. *Bulletin of the Japan Society of Mechanical Engineers*, 16(99), 1254-62.

Pavier, E., Doremus, P. (1999). Triaxial characterization of iron powder behaviour. *Powder Metallurgy*, 42(4), 345-52.

PM Modnet Research Group. (1999). Comparison of computer models representing powder compaction process. *Powder Metallurgy*, 42(4), 301-11.

PM Modnet Research Group. (2002). Numerical simulation of powder compaction for two multilevel ferrous parts, including powder characterisation and experimental validation. *Powder Metallurgy*, 45(4), 335-44.

Rahman, M. M., Ariffin, A. K., Nor, S. S. M. (2009). Development of a finite element model of metal powder compaction process at elevated temperature. *Applied Mathematical Modeling*, 33(11), 4031-48.

Rahman, M. M., Nor, S. S. M., Rahman, H. Y. (2011). Investigation on the effect of lubrication and forming parameters to the green compact generated from iron powder through warm forming route. *Materials and Design*, 32, 447-52.

Roscoe, K. H., Schofield, A. N., Thurairajah, A. (1963). Yielding of clays in states wetter than critical. *Geotéchnique*, 13, 211-40.

Sandler, I. S., Rubin, D. (1979). An algorithm and a modular subroutine for the cap model. *International Journal for Numerical and Analytical Methods in Geomechanics*, 3(2), 173-86.

Shima, S., Saleh, M. A. E. (1993). Variation of density distribution in compacts in closed-die compaction with powder characteristics. *Advances in Powder Metallurgy & Particulate Materials, 3, Modeling, Design, and Computational Methods*, 175-88.

Shtern, M. B., Mikhailov, O. V. (2002). Numerical modeling of the compaction of powder articles of complex shape in rigid dies: effect of pressing method on density distribution 1. Mechanical model of powder densification. *Powder Metallurgy and Metal Ceramics*, 41(11-12), 581-7.

Sinka, I. C. (2007). Modelling powder compaction. *KONA*, 25, 4-22.

Sinka, I. C., Cocks, A. C. F., Morrison, C. J., Lightfoot, A. (2000). High pressure triaxial facility for powder compaction. *Powder Metallurgy*, 43(3), 253-62.

Smith, L. N., Midha, P. S., Graham, A. D. (1998). Simulation of metal powder compaction, for the development of a knowledge based powder metallurgy process advisor. *Journal of Materials Processing Technology*, 79(1), 94-100.

Svoboda, A., Haggblad, H., Nasstrom, M. (1996). Simulation of hot isostatic pressing of metal powder components to near net shape. *Engineering Computations*, 13(5), 13-37.

Tran, D. V., Lewis, R. W., Gethin, D. T., Ariffin, A. K. (1993). Numerical modelling of powder compaction processes: Displacement based finite element method. *Powder Metallurgy*, 36(4), 257-66.

Tresca, H. (1864). Sur I'ecoulement des corps solids soumis a de fortes pression. *Comptes Rendus hebdomadaires des Seances de l'Academie des Sciences*, Rend 59, 754–8.

von Mises, R. (1913). Mechanik der Festen Körper im plastisch deformablen Zustand. *Nachrichten von der Königlichen Gesellschaft der wissenschaften zu Göettinger, Mathematisch-physikalische Klasse*, 1, 582–92.

Weber, G. G., Brown, S. B. (1989). Simulation of the compaction of powder components. *Advances in Powder Metallurgy and Particulate Materials* 1, 105-18.

Wikman, B., Bergman, G., Oldenburg, M., Haggblad, H. (2006). Estimation of constitutive parameters for powder pressing by inverse modelling. *Structural and Multidisciplinary Optimization*, 31(5), 400-9.

Wikman, B., Solimannezhad, N., Larsson, R., Oldenburg, M., Haggblad, H. (2000). Wall friction coefficient estimation through modelling of powder die pressing experiment. *Powder Metallurgy*, 43(2), 132-8.

Zadeh, H., Kim, I. Y., Jeswiet, J. (2009). Nonlinear finite element analysis of metal powder die compaction using various plasticity models. *Transactions of the NAMRI/SME*, 37, 357-63.

Zhou, Z., Zhao, W., Chen, P., Chen, W., Shao, M., Wang, J. (2002). Simulation of die wall friction's effect on density distribution in metallic powder compaction. *Transactions of the Nonferrous Metals Society of China*, 12(5), 890-3.

Zhu, Y., Li, J., Liang, D., Xiang, Z., Yin, Z. (2012). Comparison study of single direction and friction assisted compaction of multiple alloy powders by finite element simulation. *Powder Metallurgy and Metal Ceramics*, 50(9-10), 586-95.

Appendix A: LS-DYNA Code for 300 MPa Compaction

dcompaction.dyn

```
$ Units
$---+----1----+----2----+----3----+----4----+----5----+----6----+----7----+----8
$   LENGTH      MASS      TIME     FORCE    STRESS    ENERGY     POWER   DENSITY
$      [m]      [kg]       [s]       [N]      [Pa]       [J]       [W]   [kg/m3]
$
$
*KEYWORD_ID
$---+----1----+----2----+----3----+----4----+----5----+----6----+----7----+----8
$           PROJECT                 NUM                                   STAGE
DIECOMP             SELIG_SA_300MPa    RIGIDPUNCH_ELFORM15
$
$
$---+----1----+----2----+----3----+----4----+----5----+----6----+----7----+----8
$                                                                             $
$                          PARAMETER DEFINITIONS                              $
$                                                                             $
$---+----1----+----2----+----3----+----4----+----5----+----6----+----7----+----8
*PARAMETER
$---+----1----+----2----+----3----+----4----+----5----+----6----+----7----+----8
$    PRMR1      VAL1     PRMR2      VAL2     PRMR3      VAL3     PRMR4      VAL4
R ENDTIM     +0.0450R HLDTIM     +0.0400R DTOUT      +0.0020R MAXDISP     -0.001
$    PRMR5      VAL5     PRMR6      VAL6     PRMR7      VAL7     PRMR8      VAL8
R LOAD        -53014R FRIC       +0.2400R SFACT         5.00
$
$
*TITLE
Single-Action Die Compaction (300MPa)
$
$
$---+----1----+----2----+----3----+----4----+----5----+----6----+----7----+----8
$                                                                             $
$                                  CONTROL CARD                               $
$                                                                             $
$---+----1----+----2----+----3----+----4----+----5----+----6----+----7----+----8
*CONTROL_TIMESTEP
$---+----1----+----2----+----3----+----4----+----5----+----6----+----7----+----8
$   DTINIT    TSSFAC      ISDO    TSLIMT     DT2MS      LCTM     ERODE     MS1ST
         0       0.8         0       0.0       0.0         0         0         0
$---+----1----+----2
$   DT2MSF   DT2MSLC

$
$
*CONTROL_TERMINATION
$---+----1----+----2----+----3----+----4----+----5
$   ENDTIM    ENDCYC     DTMIN    ENDENG    ENDMAS
&ENDTIM            0       0.0       0.0       0.0
$
$
*CONTROL_ENERGY
$---+----1----+----2----+----3----+----4
$     HGEN      RWEN    SLNTEN     RYLEN
         2         1         2         1
$
$
*CONTROL_HOURGLASS
```

```
$---+----1----+----2
$      IHQ        QH
         1      0.10
$
$
$---+----1----+----2----+----3----+----4----+----5----+----6----+----7----+----8
$                                                                              $
$                         DATABASE CONTROL FOR BINARY                          $
$                                                                              $
$---+----1----+----2----+----3----+----4----+----5----+----6----+----7----+----8
*DATABASE_BINARY_D3PLOT
$---+----1----+----2----+----3----+----4
$  DT/CYCL      LCDT      BEAM     NPLTC
&DTOUT             0         0         0
$---+----1
$    IOOPT
         0
$
$
*DATABASE_RCFORC
$---+----1----+----2
$       DT    BINARY
&DTOUT             1
$
$
*DATABASE_GLSTAT
$---+----1----+----2
$       DT    BINARY
&DTOUT             1
$
$
*DATABASE_MATSUM
$---+----1----+----2
$       DT    BINARY
&DTOUT             1
$
$
*DATABASE_RBDOUT
$---+----1----+----2
$       DT    BINARY
&DTOUT             1
$
$
$---+----1----+----2----+----3----+----4----+----5----+----6----+----7----+----8
$                                                                              $
$                                  PART CARDS                                  $
$                                                                              $
$---+----1----+----2----+----3----+----4----+----5----+----6----+----7----+----8
*INCLUDE
7n5mm_die_0n500mm_elems_10g_sample_SELIG.mesh
$
$
*INCLUDE
matdef.dyn
$
$
*INCLUDE
die.part
$
$
*INCLUDE
toppunch.part
$
$
*INCLUDE
bottompunch.part
$
$
*INCLUDE
sample.part
$
```

```
$
*SET_PART_LIST
$MASTERS, DIE AND PUNCH
$---+----1----+----2----+----3----+----4----+----5----+----6----+----7----+----8
$      SID       DA1       DA2       DA3       DA4
         1
$     PID1      PID2      PID3      PID4      PID5      PID6      PID7      PID8
         1
$
$
*SET_PART_LIST
$MASTERS, DIE AND PUNCH
$---+----1----+----2----+----3----+----4----+----5----+----6----+----7----+----8
$      SID       DA1       DA2       DA3       DA4
         2
$     PID1      PID2      PID3      PID4      PID5      PID6      PID7      PID8
         2
$
$
*SET_PART_LIST
$MASTERS, DIE AND PUNCH
$---+----1----+----2----+----3----+----4----+----5----+----6----+----7----+----8
$      SID       DA1       DA2       DA3       DA4
         4
$     PID1      PID2      PID3      PID4      PID5      PID6      PID7      PID8
         4
$
$
*SET_PART_LIST
$SLAVE, POWDER
$---+----1----+----2----+----3----+----4----+----5----+----6----+----7----+----8
$      SID       DA1       DA2       DA3       DA4
         3
$     PID1      PID2      PID3      PID4      PID5      PID6      PID7      PID8
         3
$
$---+----1----+----2----+----3----+----4----+----5----+----6----+----7----+----8
$                                                                             $
$                              CONTACT CARDS                                  $
$                                                                             $
$---+----1----+----2----+----3----+----4----+----5----+----6----+----7----+----8
*CONTACT_2D_AUTOMATIC_SURFACE_TO_SURFACE
$---+----1----+----2----+----3----+----4----+----5----+----6----+----7----+----8
$     SIDS      SIDM     SFACT      FREQ        FS         FD         DC     MEMBS
         3         1&SFACT            50&FRIC
$---+----1----+----2----+----3----+----4----+----5----+----6----+----7----+----8
$   TBIRTH    TDEATH       SOS       SOM       NDS       NDM       COF      INIT
                                                                            1
$
*CONTACT_2D_AUTOMATIC_SURFACE_TO_SURFACE
$---+----1----+----2----+----3----+----4----+----5----+----6----+----7----+----8
$     SIDS      SIDM     SFACT      FREQ        FS         FD         DC     MEMBS
         3         2&SFACT            50&FRIC
$---+----1----+----2----+----3----+----4----+----5----+----6----+----7----+----8
$   TBIRTH    TDEATH       SOS       SOM       NDS       NDM       COF      INIT
                                                                            1
$
*CONTACT_2D_AUTOMATIC_SURFACE_TO_SURFACE
$---+----1----+----2----+----3----+----4----+----5----+----6----+----7----+----8
$     SIDS      SIDM     SFACT      FREQ        FS         FD         DC     MEMBS
         3         4&SFACT            50&FRIC
$---+----1----+----2----+----3----+----4----+----5----+----6----+----7----+----8
$   TBIRTH    TDEATH       SOS       SOM       NDS       NDM       COF      INIT
                                                                            1
$
$
$
$---+----1----+----2----+----3----+----4----+----5----+----6----+----7----+----8
$                                                                             $
$                          MOTION/DYNAMICS CARDS                              $
$                                                                             $
```

```
$---+----1----+----2----+----3----+----4----+----5----+----6----+----7----+----8
*LOAD_RIGID_BODY
$---+----1----+----2----+----3----+----4----+----5----+----6----+----7----+----8
$      PID       DOF      LCID        SF       CID        M1        M2        M3
         2         2         1&LOAD
$
$
$---+----1----+----2----+----3----+----4----+----5----+----6----+----7----+----8
$                                                                               $
$                               LOAD CURVE CARDS                                $
$                                                                               $
$---+----1----+----2----+----3----+----4----+----5----+----6----+----7----+----8
*DEFINE_CURVE
$---+----1----+----2----+----3----+----4----+----5----+----6----+----7
$     LCID      SIDR       SFA       SFO      OFFA      OFFO    DATTYP
         1         0      +1.0      +1.0       0.0       0.0         0
$---+----1----+----2----+----3----+----4
$            XVALUES            YVALUES
          +0.000E+00          +0.000E+00
&HLDTIM                       +1.000E+00
&ENDTIM                       +1.000E+00
$
$
$---+----1----+----2----+----3----+----4----+----5----+----6----+----7----+----8
$
$
$---+----1----+----2----+----3----+----4----+----5----+----6----+----7----+----8
$                                                                               $
$                           IMPLICIT SPRINGBACK                                 $
$                                                                               $
$---+----1----+----2----+----3----+----4----+----5----+----6----+----7----+----8
*INTERFACE_SPRINGBACK_LSDYNA
$---+----1----+----2----+----3----+----4----+----5----+----6----+----7
$     PSID      NSHV     FTYPE              FTENSR
         3        15         2                   0
$
$
*END
```

matdef.dyn

```
*KEYWORD
$---+----1----+----2----+----3----+----4----+----5----+----6----+----7----+----8
$                                                                               $
$                              MATERIAL KEYWORDS                                $
$                                                                               $
$---+----1----+----2----+----3----+----4----+----5----+----6----+----7----+----8
*MAT_ELASTIC_TITLE
$---+----1
$  HEADING
ALUMINUM
$---+----1----+----2----+----3----+----4----+----5----+----6----+----7
$      MID        RO         E        PR        DA        DB         K
         1      2680  71.0E+09     0.334
$
$
*MAT_RIGID_TITLE
$---+----1
$  HEADING
STEEL,DIE
$---+----1----+----2----+----3----+----4----+----5----+----6----+----7----+----8
$      MID        RO         E        PR         N    COUPLE         M     ALIAS
         2      7800 210.0E+09      0.29
$---+----1----+----2----+----3
$      CMO      CON1      CON2
      +1.0       7.0       7.0
$---+----1----+----2----+----3----+----4----+----5----+----6
$   LCO/A1        A2        A3        V1        V2        V3
```

```
$
$
*MAT_RIGID_TITLE
$---+----1
$  HEADING
STEEL,PUNCH
$---+----1----+----2----+----3----+----4----+----5----+----6----+----7----+----8
$      MID        RO         E        PR         N    COUPLE         M     ALIAS
         3      7800 210.0E+09      0.29
$---+----1----+----2----+----3
$      CMO      CON1      CON2
      +1.0       6.0       7.0
$---+----1----+----2----+----3----+----4----+----5----+----6
$   LCO/A1        A2        A3        V1        V2        V3

$
$
*MAT_GEOLOGIC_CAP_MODEL_TITLE
$ Al6061 (Lee and Kim)
$ THEORETICAL MAX DENSITY = 2700 KG/M3
$ RO - 44.7% of max density. BULK and G - 44.7% of values from matweb. GAMMA and BETA =
0? TOFF = ???
$---+----1
$  HEADING
AL6061
$---+----1----+----2----+----3----+----4----+----5----+----6----+----7----+----8
$      MID        RO      BULK         G     ALPHA     THETA     GAMMA      BETA
        13      1207  48.87E+9  11.62E+9         0     0.394         0         0
$---+----1----+----2----+----3----+----4----+----5----+----6
$        R         D         W        X0         C         N
     2.800    1.4E-9      0.76
$---+----1----+----2----+----3----+----4
$     PLOT     FTYPE       VEC      TOFF
       3.0       1.0       0.0 -2.068E+6
$
*END
```

die.part

```
*KEYWORD
$---+----1----+----2----+----3----+----4----+----5----+----6----+----7----+----8
$                                                                             $
$                                PART KEYWORDS                                $
$                                                                             $
$---+----1----+----2----+----3----+----4----+----5----+----6----+----7----+----8
*PART
$---+----1
$  HEADING
DIE
$---+----1----+----2----+----3----+----4----+----5----+----6----+----7----+----8
$      PID     SECID       MID     EOSID      HGID      GRAV    ADPOPT      TMID
         1         1         2         0         0         0         0         0
$
$
$---+----1----+----2----+----3----+----4----+----5----+----6----+----7----+----8
$                                                                             $
$                              SECTION KEYWORDS                               $
$                                                                             $
$---+----1----+----2----+----3----+----4----+----5----+----6----+----7----+----8
*SECTION_SHELL
$---+----1
$  HEADING
$SOLID, DIE
$---+----1----+----2----+----3----+----4----+----5----+----6----+----7----+----8
$    SECID    ELFORM      SHRF       NIP     PROPT   QR/IRID     ICOMP     SETYP
         1        15       1.0         2       0.0       0.0         0         1
$
```

```
$---+----1----+----2----+----3----+----4----+----5----+----6----+----7----+----8
$       T1        T2        T3        T4      NLOC     MAREA      IDOF    EDGSET
       0.0       0.0       0.0       0.0       0.0       0.0       0.0
$
*END
```

toppunch.part

```
*KEYWORD
$---+----1----+----2----+----3----+----4----+----5----+----6----+----7----+----8
$                                                                             $
$                                PART KEYWORDS                                $
$                                                                             $
$---+----1----+----2----+----3----+----4----+----5----+----6----+----7----+----8
*PART
$---+----1
$  HEADING
TOPPUNCH
$---+----1----+----2----+----3----+----4----+----5----+----6----+----7----+----8
$      PID     SECID       MID     EOSID      HGID      GRAV    ADPOPT      TMID
         2         2         3         0         0         0         0         0
$
$
$---+----1----+----2----+----3----+----4----+----5----+----6----+----7----+----8
$                                                                             $
$                              SECTION KEYWORDS                               $
$                                                                             $
$---+----1----+----2----+----3----+----4----+----5----+----6----+----7----+----8
*SECTION_SHELL
$---+----1
$  HEADING
$SOLID, PUNCH
$---+----1----+----2----+----3----+----4----+----5----+----6----+----7----+----8
$    SECID    ELFORM      SHRF       NIP     PROPT   QR/IRID     ICOMP     SETYP
         2        15       1.0         2       0.0       0.0         0         1
$
$---+----1----+----2----+----3----+----4----+----5----+----6----+----7----+----8
$       T1        T2        T3        T4      NLOC     MAREA      IDOF    EDGSET
       0.0       0.0       0.0       0.0       0.0       0.0       0.0
$
$
*END
```

bottompunch.part

```
*KEYWORD
$---+----1----+----2----+----3----+----4----+----5----+----6----+----7----+----8
$                                                                             $
$                                PART KEYWORDS                                $
$                                                                             $
$---+----1----+----2----+----3----+----4----+----5----+----6----+----7----+----8
*PART
$---+----1
$  HEADING
BOTTOMPUNCH
$---+----1----+----2----+----3----+----4----+----5----+----6----+----7----+----8
$      PID     SECID       MID     EOSID      HGID      GRAV    ADPOPT      TMID
         4         4         2         0         0         0         0         0
$
$
$---+----1----+----2----+----3----+----4----+----5----+----6----+----7----+----8
$                                                                             $
$                              SECTION KEYWORDS                               $
$                                                                             $
$---+----1----+----2----+----3----+----4----+----5----+----6----+----7----+----8
```

```
*SECTION_SHELL
$---+----1
$  HEADING
$SOLID, PUNCH
$---+----1----+----2----+----3----+----4----+----5----+----6----+----7----+----8
$    SECID    ELFORM      SHRF       NIP     PROPT   QR/IRID     ICOMP     SETYP
         4        15       1.0         2       0.0       0.0         0         1
$
$---+----1----+----2----+----3----+----4----+----5----+----6----+----7----+----8
$       T1        T2        T3        T4      NLOC     MAREA      IDOF    EDGSET
      0.0       0.0       0.0       0.0       0.0       0.0       0.0
$
$
*END
```

sample.part

```
*KEYWORD
$---+----1----+----2----+----3----+----4----+----5----+----6----+----7----+----8
$                                                                             $
$                                PART KEYWORDS                                $
$                                                                             $
$---+----1----+----2----+----3----+----4----+----5----+----6----+----7----+----8
*PART
$---+----1
$  HEADING
POWDER
$---+----1----+----2----+----3----+----4----+----5----+----6----+----7----+----8
$      PID     SECID       MID     EOSID      HGID      GRAV    ADPOPT      TMID
         3         3        13         0         0         0         0         0
$
$
$---+----1----+----2----+----3----+----4----+----5----+----6----+----7----+----8
$                                                                             $
$                             SECTION KEYWORDS                                $
$                                                                             $
$---+----1----+----2----+----3----+----4----+----5----+----6----+----7----+----8
*SECTION_SHELL
$---+----1
$  HEADING
$SOLID, POWDER
$---+----1----+----2----+----3----+----4----+----5----+----6----+----7----+----8
$    SECID    ELFORM      SHRF       NIP     PROPT   QR/IRID     ICOMP     SETYP
         3        15       1.0         2       0.0       0.0         0         1
$
$---+----1----+----2----+----3----+----4----+----5----+----6----+----7----+----8
$       T1        T2        T3        T4      NLOC     MAREA      IDOF    EDGSET
      0.0       0.0       0.0       0.0       0.0       0.0       0.0
$
$
*END
```

Appendix B: LS-DYNA Code for 300 MPa Springback

dcompaction_springback.dyn

```
*KEYWORD
$
*KEYWORD_ID
$---+----1----+----2----+----3----+----4----+----5----+----6----+----7----+----8
$            PROJECT                NUM                                  STAGE
DIECOMP_SPRINGBACK  SINGLEACT_300MPa    RIGIDPUNCH_ELFORM15
$
$
*TITLE
SINGLE_ACTION_SPRINGBACK
$
$
$--------------
$
*INCLUDE
DIECOMP_SELIG_SA_300MPa_RIGIDPUNCH_ELFORM15.dynain
$
*INCLUDE
matdef.dyn
$
*INCLUDE
sample_springback.part
$
$--------------
$
*CONTROL_IMPLICIT_GENERAL
$   imflag       dt0      iefs
         1    0.2500         0
$
*CONTROL_IMPLICIT_SOLUTION
$  nlsolvr    ilimit    maxref     dctol     ectol     rctol     lstol    abstol
         2        11        15     0.001      0.01   1.0E+10       0.9   1.0E-10
$    dnorm   divflag   inistif   nlprint
         2         1         1         0
$
*CONTROL_IMPLICIT_AUTO
$    iauto    iteopt    itewin     dtmin     dtmax
         0        11         5   0.00025       2.5
$
*CONTROL_IMPLICIT_STABILIZATION
$      ias     scale    tstart      tend
         0       0.0         0         0
$        1      0.00         0         0
$
$--------------
$
*CONTROL_TERMINATION
      3.00
$
*DATABASE_BINARY_D3PLOT
      0.01
$
$--------------
$
*END
```

matdef.dyn

$

```
*KEYWORD
$---+----1----+----2----+----3----+----4----+----5----+----6----+----7----+----8
$                                                                             $
$                              MATERIAL KEYWORDS                              $
$                                                                             $
$---+----1----+----2----+----3----+----4----+----5----+----6----+----7----+----8
*MAT_ELASTIC_TITLE
$---+----1
$  HEADING
ALUMINUM
$---+----1----+----2----+----3----+----4----+----5----+----6----+----7
$      MID        RO         E        PR        DA        DB         K
         1      2680  71.0E+09     0.334
$
$
*MAT_RIGID_TITLE
$---+----1
$  HEADING
STEEL,DIE
$---+----1----+----2----+----3----+----4----+----5----+----6----+----7----+----8
$      MID        RO         E        PR         N    COUPLE         M     ALIAS
         2      7800 210.0E+09      0.29
$---+----1----+----2----+----3
$      CMO      CON1      CON2
      +1.0       7.0       7.0
$---+----1----+----2----+----3----+----4----+----5----+----6
$   LCO/A1        A2        A3        V1        V2        V3

$
$
*MAT_RIGID_TITLE
$---+----1
$  HEADING
STEEL,PUNCH
$---+----1----+----2----+----3----+----4----+----5----+----6----+----7----+----8
$      MID        RO         E        PR         N    COUPLE         M     ALIAS
         3      7800 210.0E+09      0.29
$---+----1----+----2----+----3
$      CMO      CON1      CON2
      +1.0       6.0       7.0
$---+----1----+----2----+----3----+----4----+----5----+----6
$   LCO/A1        A2        A3        V1        V2        V3

$
$
*MAT_GEOLOGIC_CAP_MODEL_TITLE
$ Al6061 (Lee and Kim)
$ THEORETICAL MAX DENSITY = 2700 KG/M3
$ RO - 44.7% of max density. BULK and G - 44.7% of values from matweb. GAMMA and BETA =
0? TOFF = ???
$---+----1
$  HEADING
AL6061
$---+----1----+----2----+----3----+----4----+----5----+----6----+----7----+----8
$      MID        RO      BULK         G     ALPHA     THETA     GAMMA      BETA
        13      1207  48.87E+9  11.62E+9         0     0.394         0         0
$---+----1----+----2----+----3----+----4----+----5----+----6
$        R         D         W        X0         C         N
     2.800     5E-10      0.62
$---+----1----+----2----+----3----+----4
$     PLOT     FTYPE       VEC      TOFF
       3.0       1.0       0.0 -2.068E+6
```

```
$
*MAT_ELASTIC_TITLE
$---+----1
$  HEADING
ELASTIC Al6061
$ RO is final bulk density; E ASSUMED TO BE calculated as rel dens at end of compaction *
72.27E+09 (94.4%) ; PR = 0.30
$---+----1----+----2----+----3----+----4----+----5----+----6----+----7
$      MID        RO         E        PR        DA        DB         K
        14      2549 68.22E+09      0.30
$
*END
```

sample_springback.part

```
*KEYWORD
$---+----1----+----2----+----3----+----4----+----5----+----6----+----7----+----8
$                                                                             $
$                                PART KEYWORDS                                $
$                                                                             $
$---+----1----+----2----+----3----+----4----+----5----+----6----+----7----+----8
*PART
$---+----1
$  HEADING
POWDER
$---+----1----+----2----+----3----+----4----+----5----+----6----+----7----+----8
$      PID     SECID       MID     EOSID      HGID      GRAV    ADPOPT      TMID
         3         3        14         0         0         0         0         0
$
$
$---+----1----+----2----+----3----+----4----+----5----+----6----+----7----+----8
$                                                                             $
$                              SECTION KEYWORDS                               $
$                                                                             $
$---+----1----+----2----+----3----+----4----+----5----+----6----+----7----+----8
*SECTION_SHELL
$---+----1
$  HEADING
$SOLID, POWDER
$---+----1----+----2----+----3----+----4----+----5----+----6----+----7----+----8
$    SECID    ELFORM      SHRF       NIP     PROPT   QR/IRID     ICOMP      SETYP
         3        15       1.0         2       0.0       0.0         0          1
$
$---+----1----+----2----+----3----+----4----+----5----+----6----+----7----+----8
$       T1        T2        T3        T4      NLOC     MAREA      IDOF    EDGSET
      0.0       0.0       0.0       0.0       0.0       0.0       0.0
$
$
*END
```